Mon. Not. R. Astron. Soc. **383,** 1619–1638 (2008) doi:10.1111/j.1365-2966.2007.12682.x

Regular black hole motion and stellar orbital resonances

C. M. Boily,[1⋆] T. Padmanabhan[2] and A. Paiement[3]

[1]*Observatoire astronomique & CNRS UMR 7550, Université de Strasbourg I, 11 rue de l'université, F-67000 Strasbourg, France*
[2]*IUCAA, Ganeshkhind Post Bag 4, Pune, India*
[3]*ENSP de Strasbourg, Parc d'innovation, Bd. Sébastien Brant BP 10413, F-67412 Illkirch, France*

Accepted 2007 November 3. Received 2007 October 31; in original form 2007 June 2

ABSTRACT

The motion of a black hole about the centre of gravity of its host galaxy induces a strong response from the surrounding stellar population. We treat the case of a harmonic potential analytically and show that half of the stars on circular orbits in that potential shift to an orbit of lower energy, while the other half receive a positive boost and recede to a larger radius. The black hole itself remains on an orbit of fixed amplitude and merely acts as a catalyst for the evolution of the stellar energy distribution function $f(E)$. We show that this effect is operative out to a radius of approximately three to four times the hole's influence radius, $R_{\rm bh}$. We use numerical integration to explore more fully the response of a stellar distribution to black hole motion. We consider orbits in a logarithmic potential and compare the response of stars on circular orbits, to the situation of a 'warm' and 'hot' (isotropic) stellar velocity field. While features seen in density maps are now wiped out, the kinematic signature of black hole motion still imprints the stellar line-of-sight mean velocity to a magnitude $\simeq$13 per cent the local rms velocity dispersion σ. A study in three dimensions suggests a reduced effect for polar orbits.

Key words: gravitation – stellar dynamics – Galaxy: centre – galaxies: nuclei.

1 INTRODUCTION

Black hole (BH) dynamics in galactic nuclei has attracted much attention for many years (e.g. Begelman, Blandford & Rees 1984; Kormendy & Richstone 1995; Merritt 2006, for a recent review). The influence of a BH on its surrounding stars is felt first through the large velocity dispersion and rapid orbital motion of the innermost cluster stars ($\sigma \sim v_{\rm 1d} \lesssim 10^3$ km s^{-1}). This sets a scale $\lesssim GM_{\rm bh}/\sigma^2$ ($\simeq$0.015–0.019 pc for the Milky Way, henceforth MW) within which high-angle scattering or stellar stripping and disruption may take place. For the MW, low-impact parameter star–BH encounters are likely, given the high density of $\rho \sim 10^7\,{\rm M}_\odot\,{\rm pc}^{-3}$ within a radius of approximately a few pc (see e.g. Yu & Tremaine 2003; O'Leary & Loeb 2007; see also Freitag, Amaro-Seoane & Kalogera 2006 for a numerical approach to this phenomenon). Star–BH scattering occurring over a relaxation time (Preto, Merritt & Spurzem 2004 and references therein; Binney & Tremaine 1987) leads to the formation of a Bahcall–Wolf stellar cusp of density $\rho_\star \sim r^{-\gamma}$, where γ falls in the range 3/2–7/4 (Bahcall & Wolf 1977). Genzel et al. (2003) modelled the kinematics of the inner few parsecs of Sgr A$_\star$ with a mass profile $\rho_\star \sim r^{-1.4}$, suggestive of a strong interplay between the BH and the central stellar cusp. More recently, Schödel et al. (2007) presented a double power-law fit to the data, where the power index $\simeq$1.2 inside a breaking radius $r_{\rm br} \simeq 0.2$ pc, and $\simeq$7/4 outside. This is indicative of ongoing evolution on a scale $\sim r_{\rm br}$ not accounted for in the Bahcall–Wolf solution.

Most, if not all, studies of galactic nucleus dynamics assume a fixed BH (or BH binary) at the centre of coordinates. Genzel et al. (1997) had set a constraint of $\lesssim$10 km s^{-1} for the speed of the BH relatively to the Galactic plane, a constraint later refined to $\lesssim$2 km^{-1} (Backer & Sramek 1999; Reid & Brunthaler 2004). Stellar dynamics on scales of approximately a few pc surrounding Sgr A$_\star$ is complex, however, and the angular momentum distribution on that scale is a prime example of this complexity (Genzel et al. 2003). Reid et al. (2007) used maser emission maps to compute the mean velocity of 15 SiO emitters relatively to Sgr A$_\star$. They compute a mean (three-dimensional) velocity of up to 45 km s^{-1}, a result obtained from sampling a volume of $\simeq$1 pc about the centre.[1] This raises the possibility that stars within the central stellar cusp experience significant streaming motion with respect to Sgr A$_\star$. The breaking radius $r_{\rm br} \sim 0.2$ pc is suggestive of uncertain dynamics on that scale. Random, 'Brownian' BH motion may result from the expected high-deflection-angle encounters (Merritt 2001, 2005; Merritt, Berczik & Laun 2007). Here, we take an alternative approach, and ask what net effect a BH set on a regular orbit will have on the stars. In doing so, we aim to fill an apparent gap in the modelling of BH dynamics

⋆E-mail: cmb@astro.u-strasbg.fr

[1] Statistical root-n noise $\sim$25 per cent remains large owing to the small number of sources but is of no consequence to the argument being developed here.

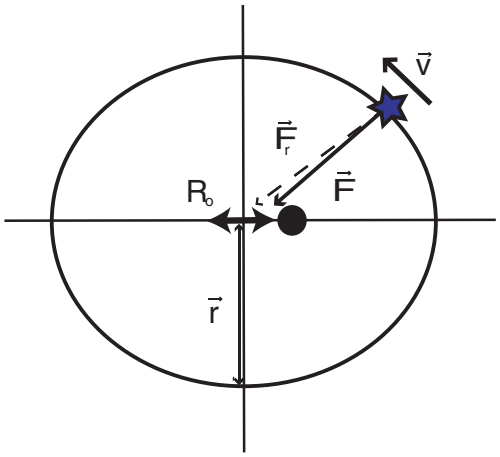

Figure 1. Cartoon representing a star on a circular orbit in the combined potential of a BH and a background galaxy. The BH motion of amplitude R_o runs parallel to the horizontal x-axis. The net force $\boldsymbol{F}$ acting on the star may be decomposed into a radial component $\boldsymbol{F}_r$ and an x-component.

in dense nuclei, by relaxing further the constraint that the hole be held fixed at the centre of coordinates.

A rough calculation will help to get some orientation into the problem. Consider a BH falling from rest from a radius R_o in the background potential of the MW stellar cusp. Let the radial mass profile of the cusp $\rho_\star(r) \propto r^{-3/2}$, consistent with MW kinematic data. If we define the BH radius of influence $\simeq$1 pc to be the radius where the integrated mass $M_\star(< r)$ is equal to the BH mass $\simeq$3–$4 \times 10^6\,\mathrm{M}_\odot$ (Genzel et al. 2003; Ghez et al. 2005), then R_o may be expressed in terms of the maximum speed of the BH as it reaches the centre of the MW potential as

$$\left(\frac{\max\{v\}}{100\,\mathrm{km\,s^{-1}}}\right)^{\frac{4}{5}} = \frac{R_o}{1\,\mathrm{pc}}.$$

For a maximum velocity in the range 10–40 km s^{-1}, we find $R_o \simeq$ 0.3–0.5 pc, or the same fraction of its radius of influence.[2] We ask what impact this motion might have on the surrounding stars. To proceed further, let us focus on a circular stellar orbit outside R_o in the combined potential of the BH and an axisymmetric galaxy. Fig. 1 gives a clue to the analysis. When the BH is at rest at the centre of coordinates, the star continues on a closed circular orbit of radius r and constant velocity v. We now set the BH on a radial path of amplitude R_o down the horizontal x-axis. Let the periodic orbits of the star and BH have an angular frequency ω, and the motion of the bodies be out of phase by $\phi_o \in [0, 2\pi]$. The net force $\boldsymbol{F}$ acting on the star can always be expressed as the sum of a radial component $\boldsymbol{F}_r$ and a force parallel to the x-axis, which we take to be of the form $F_x \cos(\omega t + \phi_o)$; clearly, the constant $F_x = 0$ when $R_o = 0$. The net mechanical work done on the star by the BH as the star completes one orbit is the integral $\delta W = \int \boldsymbol{F} \cdot \boldsymbol{v}\,\mathrm{d}t$. We show in Section 2 that δW changes sign but keeps the same amplitude when the phase ϕ_o shifts to $\phi_o + \pi$. Thus, whenever the stellar phase-space density is well sampled and all values of the angle ϕ_o are realized with equal probability, half the stars will receive ($\delta W > 0$) mechanical energy from, and half will give off ($\delta W < 0$) energy to, the BH. In other words, stars in the first quadrant of a Cartesian grid will exchange energy with those in the third quadrant (similarly for those in the second and fourth quadrants). By construction, the BH's energy budget amounts to zero: it neither gains nor loses energy. For that reason, we will say that the hole acts as a *catalyst* for the redistribution of mechanical energy between the stars. Our goal then is to explore the consequences of this mechanism quantitatively for realistic stellar distribution functions.

We begin with an analysis of star–BH orbit coupling in a harmonic (uniform density) galactic potential (Section 2). While this choice may appear artificial and an oversimplification, it circumscribes all latitude allowed by uncertainties in the spatial distribution of stars within the BH influence radius. Furthermore, the basic mechanics is more tractable for that case. This is then extended to the case of a logarithmic potential (Sections 3 and 4). To cover a wider range of parameters, we explore with a response code the evolution of individual orbits in the time-dependent potential. We show that BH motion shapes up the energy distribution function, as well as the line-of-sight velocity $v_{1\mathrm{d}}$, which we measure as rms deviations from expected values. The magnitude of these deviations rise monotonically with the amplitude of the BH's orbit, and its mass. Finally, in Section 5 we discuss some applications and explore possible extensions to our analysis.

2 CIRCULAR ORBITS IN A HARMONIC POTENTIAL

We start with the case of a star initially on a circular path in a background harmonic potential to introduce some basic results and notation. The star's orbit for that problem is obtained by solving the equations of a decoupled oscillator. In Cartesian coordinates, these read

$$\ddot{\boldsymbol{x}} = -\omega^2 \boldsymbol{x}, \tag{1}$$

where

$$\omega \equiv \sqrt{4\pi G\rho/3}$$

defines the harmonic angular frequency in an axially-symmetric galaxy of uniform density ρ. Adding a fixed BH of mass M_{bh} at the centre of the coordinates preserves the symmetry of the force field: each circular orbit of the harmonic potential maps to a circular orbit in this new potential but with an angular frequency $\omega_\star > \omega$ now a function of the radius. The aim, then, is to find out what happens once the BH is set in motion, so breaking the symmetry of the force field.

2.1 Coplanar, radial BH motion

We consider a two-dimensional system so all orbits are coplanar. Let the position vector of the BH be denoted by $\boldsymbol{R}$ and we take $M_{\mathrm{bh}} \gg m_\star$. The BH obeys the same equations (1) for any $\boldsymbol{R}$ not exceeding the uniform-density core of the model potential. (A Bahcall–Wolf cusp would soon develop around the centre once the BH has settled there; the harmonic potential would remain largely unperturbed until that happens.) We define the BH radius of influence R_{bh} such that

$$M_{\mathrm{bh}} \equiv 4\pi\rho R_{\mathrm{bh}}^3/3, \tag{2}$$

which we will use again in a study of the logarithmic potential (Section 3). The full gravitational potential

$$\Phi(\boldsymbol{r}, t) = \frac{\omega^2}{2} r^2 + \Phi_{\mathrm{bh}}(\boldsymbol{r}, t),$$

[2] These figures are robust to details of the stellar cusp mass profile, so for instance a flat density profile ($\gamma = 0$) would yield R_o in the range 0.3–0.6 pc.

where, by definition,

$$\Phi_{\rm bh}(\boldsymbol{r},t) \equiv -\frac{GM_{\rm bh}}{||\boldsymbol{r}-\boldsymbol{R}(t)||} \tag{3}$$

is an explicit function of time through $\boldsymbol{R}$. The time-derivative of the star's energy $E_{\rm J}$ per unit mass,

$$E_{\rm J} = \frac{1}{2}v^2 + \Phi(\boldsymbol{r},t), \tag{4}$$

is

$$\dot{E}_{\rm J} = \frac{\partial}{\partial t}\Phi_{\rm bh}(\boldsymbol{r},t) \neq 0,$$

so energy is not conserved on the orbit. The energy $E_{\rm J}(t)$ is found by integrating $\dot{E}_{\rm J}$ over time; to do so requires a specific solution for $R(t)$. Solving equations (1) for a radial orbit down the x-axis we write

$$\boldsymbol{R}(t) = R_{\rm o}\sin(\omega t + \phi_{\rm o})\hat{\boldsymbol{x}}, \tag{5}$$

where a hat denotes a unit vector, and $R_{\rm o}$ and $\phi_{\rm o}$ are, respectively, the amplitude and phase of the BH orbit. The total energy at time t is then

$$E_{\rm J}(t) = E_{\rm J}(0) + \int_0^t \partial_t\Phi_{\rm bh}(\boldsymbol{r},t)\,{\rm d}t \equiv E_{\rm J}(0) + \delta E_{\rm J}(t). \tag{6}$$

In general, integral (6) cannot be evaluated without knowledge of the orbital path of the star. If we imagine that the motion of the BH has little effect on the radial displacement of the star, we may compute a rough solution to equation (6) by assuming that the star follows a circular path about the centre of coordinates. The solution for $E_{\rm J}(t)$ may then be compared to equation (4) computed from the numerical integration of the equations of motion (although the approximation does not respect Hamiltonian dynamics; Appendix A addresses this issue).

When a star moves at constant $r = ||\boldsymbol{r}||$ and angular frequency $\omega_\star = {\rm d}\theta/{\rm d}t$, the position vector admits a solution of the form of equation (5) in both x- and y-coordinates but with $\omega \to \omega_\star > \omega$. The initial conditions are completely specified if we pick the phase of the stellar orbit such that the azimuthal angle $\theta = 0$ when $t = 0$ and $\boldsymbol{r} = r\hat{\boldsymbol{x}}$. Since both r and $\omega_\star = v_\theta/r$ are taken to be constant, we may write $r{\rm d}\theta = v_\theta{\rm d}t$. We define the dimensionless ratio ν of BH to star angular frequencies,

$$\nu \equiv \frac{\omega}{\omega_\star}, \tag{7}$$

which helps simplify the algebra. The ratio ν satisfies

$$\nu^{-2} = 1 + \frac{GM_{\rm bh}}{\omega^2 r^3} = 1 + \frac{M_{\rm bh}}{M_{\rm g}(<r)} \equiv \mathcal{M}, \tag{8}$$

where $\mathcal{M} \in [1,\infty[$ and $M_{\rm g}$ is the integrated galactic mass inside the orbit *of the star*. We have $\mathcal{M} = 2$ when $r = R_{\rm bh}$ by definition (2), and $\lim_{r\to\infty}\mathcal{M} = 1$.

Solving for $\delta E_{\rm J}$ in equation (6) by partial differentiation of $\Phi_{\rm bh}$, we find (see Appendix B for further details):

$$\delta E_{\rm J}(t) = \frac{GM_{\rm bh}}{r}\frac{\alpha}{\omega_\star}\int_0^\theta \dot{R}/R_{\rm o}\,{\rm d}\theta \times \frac{R/r - \cos(\theta)}{[1 + R^2/r^2 - 2(R/r)\cos(\theta)]^{\frac{3}{2}}}, \tag{9}$$

where $\theta(t) = \omega_\star t$, $\cos(\theta) = x/r$ by construction, and

$$\alpha \equiv \frac{R_{\rm o}}{r} < 1 \tag{10}$$

is a dimensionless parameter. To integrate equation (9), we substituted for $R(t) = ||\boldsymbol{R}||$ from equation (5) together with $\omega = \nu\omega_\star$ from equation (7). We did not find an exact analytical solution to the integral; however, a truncated Taylor series expansion of the potential up to third order in α (octopolar term, cf. equations B2 and B3) gives an expression in agreement with numerical integration to better than $\simeq$3 per cent for $\alpha \simeq 0.5$ or lower. In practice, we used in turn both low- and high-order Taylor series expressions for comparison with numerical integrations. Equation (9) is an implicit function of $\phi_{\rm o}$. To illustrate the relation of δE to $\phi_{\rm o}$, we graph in Fig. 2(a) the solution for eight values of $\phi_{\rm o}$ in the range $[0, 2\pi]$. Each curve is the result of integrating over one full orbit. A homogeneous sphere offers no natural scales of length or mass. We fixed units such that $G = \omega = 1$, giving an integrated mass $M_{\rm g}(<r) = r^3$; the mass of the

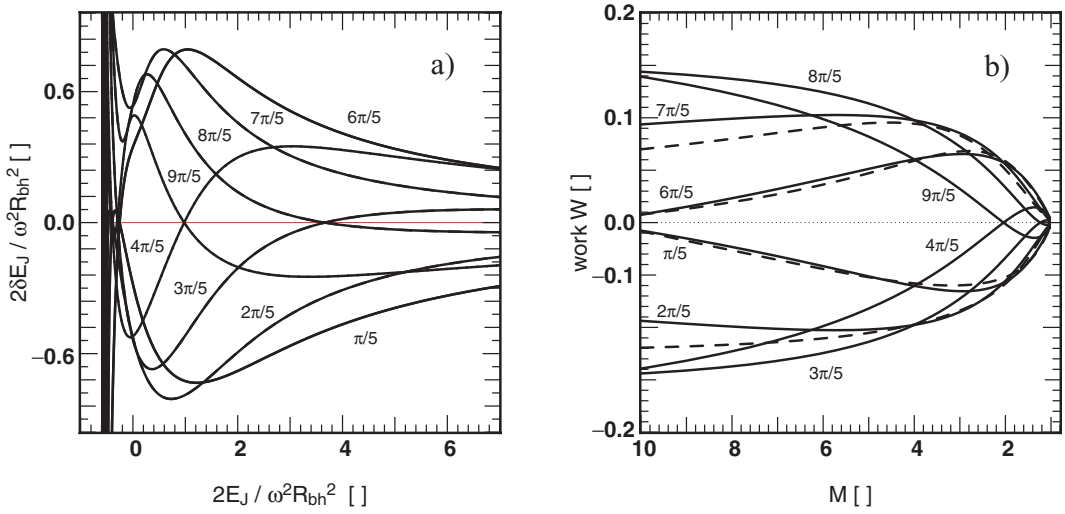

Figure 2. (a) Left-hand panel: energy increment $\delta E_{\rm J}$ for one revolution as a function of the initial orbital energy, $E_{\rm J}$. The curves are labelled with eight values of the phase angle $\phi_{\rm o}$. The calculation was done in units where $G = \omega = 1$ with a BH mass $M_{\rm bh} = 0.07$. The influence radius $R_{\rm bh} \simeq 0.42$ in those units. Both $\delta E_{\rm J}$ and $E_{\rm J}$ are given as ratios of the kinetic energy of an oscillator of amplitude $R_{\rm bh}$. (b) Right-hand panel: net work W as a function of M defined in equation (8). The solid lines is the relation (13) for the same eight values of $\phi_{\rm o}$ as in panel (a). The dash was computed using both first and second orders of a Taylor expansion, cf. equation (B6).

BH $M_{\rm bh} \approx 0.07$ gives an influence radius of $R_{\rm bh} \simeq 0.41$. Bearing in mind the constraints from Sgr A$_\star$ data (cf. Section 1), we picked a BH radial orbit of amplitude $R_{\rm o} = 0.1$, well inside $R_{\rm bh}$. The horizontal axis on Fig. 2(a) is the dimensionless energy $2E_{\rm J}/\omega^2 R_{\rm bh}^2 = 2r^2/R_{\rm bh}^2$ of the circular orbit of radius r, but shifted by -0.6 to ease comparison with the case of the logarithmic potential (see Sections 3 and 4). The radius where $r = R_{\rm o}$ (i.e. $\alpha = 1$) defines an energy of $\simeq -0.48$ in the figure. Near that point, the orbital parameters are such that the radical in equation (9) may go through zero and the integral is singular. This must occur at some value of $E_{\rm J} \approx -0.48$ for all phase angles $\phi_{\rm o}$, which is why the curves all seem to hit a wall around that value and bifurcate. By contrast, large values of $E_{\rm J}$ imply large distances from the origin. In that limit, the potential is well matched by the monopole term plus a vanishing quadrupolar correction. If we compare two curves of δE for cases where the phase angles $\phi_{\rm o}$ differ by π, we find a mirror image through the $\delta E_{\rm J} = 0$ axis. The curves of $\phi_{\rm o} = 2\pi/5$ and $7\pi/5$ are good examples of this symmetry. Thus, as long as the orbit is sufficiently far from the BH, the variation in energy along an orbit of phase angle $\phi_{\rm o}$ is opposite to that for an orbit of phase angle $\phi_{\rm o} + \pi$, as anticipated in the Introduction section. There can be no correlation between $\phi_{\rm o}$ and the star's orbital energy, and hence as many stars receive a positive energy increase as those that receive a negative contribution. This impoverishes the occupation level at $E_{\rm J}(0)$ (or, equivalently, r) and creates a hollow feature in the energy distribution function (concentric 'rings' in real space). When we move down the potential well, the curves of $\delta E_{\rm J}$ spread out progressively for all $\phi_{\rm o}$, but note that the symmetry through $\delta E_{\rm J} = 0$ is lost. For the two curves $\phi_{\rm o} = 2\pi/5$ and $7\pi/5$ and values of $2E_{\rm J}/\omega^2 R_{\rm c}^2 \approx 1$ or lower, their respective absolute values now differ by more than 0.12 (or, more than 20 per cent). This must reflect the fact that the response of the stars to the strong BH field sends them off on non-radial motion, but at a different strength according to $\phi_{\rm o}$.

To explore this aspect of the problem, we compute the mechanical work W done by the BH on a star (see also Appendix A). In an axially symmetric potential, the work done through radial motion would amount to zero after one revolution of a closed orbit, as is the case here. For that reason, we focus on the work done in azimuth. A closed integral through one revolution on the circular path $\boldsymbol{l}$ yields the net work done on the star by the time-dependent potential:

$$W = -\int \boldsymbol{\nabla}\Phi \mathrm{d}\boldsymbol{l} = -\int_0^{2\pi} \boldsymbol{\nabla}\Phi_{\rm bh}\, r\mathrm{d}\theta\, \hat{\boldsymbol{\theta}}. \tag{11}$$

We proceed as before with a limited series expansion of the potential. Appendix B gives full details of the procedure. To second-order error in $\alpha = R_{\rm o}/r$, we may write

$$\Phi_{\rm bh}(\boldsymbol{r}, t) = -\frac{GM_{\rm bh}}{r}\left(1 - \frac{1}{2}\frac{R^2 - 2xR}{r^2} + O(\alpha^2)\right). \tag{12}$$

In this limit, the force acting on the star is obtained by differentiating equation (12) with respect to $\boldsymbol{r}$ and then integrating. Doing so, and remembering equations (7) and (8), we find

$$\begin{aligned} W &= -\oint \frac{GM_{\rm bh}}{r^2}\frac{R}{r} r\mathrm{d}\theta \left(\hat{\boldsymbol{x}}\cdot\hat{\boldsymbol{\theta}}\right) = \int_0^{2\pi} \frac{GM_{\rm bh}}{r}\frac{R}{r}\sin\theta\,\mathrm{d}\theta \\ &= -\alpha\frac{GM_{\rm g}(<r)\mathcal{M}}{r}\left(\sin[\frac{2\pi}{\sqrt{\mathcal{M}}} + \phi_{\rm o}] - \sin[\phi_{\rm o}]\right). \end{aligned} \tag{13}$$

The work W given by equation (13) is a periodic function of $\phi_{\rm o} \in [0, 2\pi]$. Fig. 2(b) displays W as a function of the mass parameter $\mathcal{M}$ for several values of $\phi_{\rm o}$. The dashed curves in the figure show the result of adding the second-order term (cf. equation B6) to the first-order approximation (13). The corrections increase with $\mathcal{M}$ generally, but remain as a function of $\phi_{\rm o}$. For $\mathcal{M} = 10$, we estimate the error in W given by equation (13) to be $\simeq$20 per cent at most (see the curve labelled $2\pi/5$ in Fig. 2b). This gives confidence that the results of a low-order series expansion are already quantitatively sound when $\mathcal{M} \lesssim 4$ or so, that is, when a star orbits at a radius still well inside the influence radius $R_{\rm bh}$. Note from equation (13) that W vanishes whenever the mass parameter $\mathcal{M}$ satisfies one of the following conditions:

$$\mathcal{M} = \begin{cases} \left(\dfrac{2\pi}{\pi - 2\phi_{\rm o}}\right)^2, & \phi_{\rm o} < \dfrac{\pi}{2} \\ \left(\dfrac{2\pi}{3\pi - 2\phi_{\rm o}}\right)^2, & \dfrac{\pi}{2} \leqslant \phi_{\rm o} \leqslant \dfrac{3\pi}{2} \\ \left(\dfrac{2\pi}{5\pi - 2\phi_{\rm o}}\right)^2, & \phi_{\rm o} > \dfrac{3\pi}{2}. \end{cases} \tag{14}$$

Any star whose phase angle $\phi_{\rm o}$ and orbital radius are such that equation (14) is met possibly will not experience any or little net work as it performs one revolution about the centre.

The evolution of angular momentum $\boldsymbol{L}$ is derived from the torque $\boldsymbol{\Gamma} = \mathrm{d}\boldsymbol{L}/\mathrm{d}t = \boldsymbol{\nabla}\Phi \times \boldsymbol{r} = -GM_{\rm bh}/r^3 R(t)\sin\theta\hat{\boldsymbol{z}}$. On integrating over one (stellar) revolution, it is easy to show that $||\mathrm{d}\boldsymbol{L}|| \propto rW$. The sign of $\mathrm{d}\boldsymbol{L}$ is a function of $\phi_{\rm o}$ through W. Since the background galactic potential is taken to be axially symmetric, the distribution of angular momenta at r can be traced back directly to the characteristics of the BH orbit. It is therefore conceivable that the angular momentum of stars will be preserved if their orbit is such that $W = 0$ after each revolution.

To show that this is not the case generally, we note that as the star performs one revolution, the relative orbital phase with that of the BH will not remain constant. Under the hypothesis that the orbit is approximately circular throughout, its period remains essentially unchanged. Consequently, the relative phase angle $\phi_{\rm o}$ must shift, $\phi_{\rm o} \to \phi_{\rm o} + 2\pi\nu$, after each revolution. Thus, in that situation, the net work after n periods obtained from equation (13) amounts to

$$\begin{aligned} W_n \equiv \sum_{j=1}^{n} W_j = -\alpha\frac{GM_{\rm g}(<r)\mathcal{M}}{r}\times \\ \sum_{j=1}^{n}\left(\sin[2j\pi\nu + \phi_{\rm o}] - \sin[\phi_{\rm o} + 2(j-1)\pi\nu]\right), \end{aligned} \tag{15}$$

where $\nu = 1/\sqrt{\mathcal{M}} < 1$. Equation (15) is periodic with each n revolutions whenever $\nu = m/n$ is a rational number ($m < n$). When that is not the case, W_n never assumes twice the same value after a full cycle, but is otherwise bounded. Note that $W_n = 0$ for ν taking any positive integer value. (The case where ν is rational is discussed further in Section 4.) The same holds for the net energy, $E_{\rm J}$: the sum $E_{\rm J}(0) + \delta E_{\rm J}$ is also a periodic function of the phase angle, $\phi_{\rm o}$, as deduced from either of equations (B2) or (B3); examples are given on Figs 4 and 14 below.

By virtue of equations (8) and (13), we find in the limit $\mathcal{M} \to \infty$ (i.e. when $r \to 0$) that the work $W \propto M_{\rm g}^{-1/6} \propto r^{-1/2} \to \infty$. This result holds good independently of the different approximations used to compute W. All curves displayed in Fig. 2(b) must bifurcate for sufficiently large $\mathcal{M}$. Whenever that is the case, the orbits are quasi-Keplerian around the moving BH, and hence do not remain circular about the centre of coordinates, as we have implied so far. Our development will therefore break down when the potential is dominated by the central point source. With $\mathcal{M} = 10$, the largest value displayed on Fig. 2, the model galaxy contributes 11 per cent of the

dynamical mass only. For the MW galaxy, this would translate to a radius around Sgr A$_\star$ of $\approx$0.1 pc (Genzel et al. 2003). Stellar collisions are predicted to be important on that scale (Yu & Tremaine 2003; Merritt 2006; O'Leary & Loeb 2007). Consequently, the results presented here will only apply in the regime where the mass ratio $M_{\rm bh}/M_{\rm g} \lesssim 10$. One can deduce from equation (8) that whenever $\mathcal{M} \gg 1$, the star revolves rapidly around the BH. Such orbits remain elliptical to a good approximation when viewed in the reference frame of the BH. (The eccentricity $e = 0$ is an adiabatic invariant.) There is therefore a natural cross-over from the regime that concerns us here, to the Keplerian regime. Orbit trapping and resonant relaxation of non-circular Keplerian orbits have been discussed by various authors (e.g. Tremaine 1995; Rauch & Tremaine 1996; Zhao, Haennelt & Rees 2002; Merritt 2006).

2.2 Circular BH motion

2.2.1 Single BH

It is straightforward to extend the case of radial BH motion to one where the BH is on a circular orbit. We focus once again on the work W in the first-order approximation leading to equation (13). The results of Section 2.1 are independent of the sense of rotation of the stellar orbit. The non-zero BH angular momentum $\boldsymbol{L}_{\rm bh} = \boldsymbol{R} \times \boldsymbol{p}$ breaks this invariance. The work W will differ when stellar and BH momenta are aligned ($\boldsymbol{L}_{\rm bh} \cdot \boldsymbol{L}_\star > 0$) or anti-aligned ($\boldsymbol{L}_{\rm bh} \cdot \boldsymbol{L}_\star < 0$), as shown by, for example, Toomre & Toomre (1972) in their classic study of interacting spiral galaxies.

Consider a BH on a clockwise two-dimensional circular orbit of radius $R_{\rm o}$,

$$\boldsymbol{R}(t) = R_{\rm o}\,(\sin(\omega t + \phi_{\rm o})\,\hat{\boldsymbol{x}} + \cos(\omega t + \phi_{\rm o})\,\hat{\boldsymbol{y}}) \tag{16}$$

in a self-evident extension of equation (5). Repeating the steps leading to equation (12) will yield an extra term for the y-component but is otherwise treated identically. When computing the work (11), we may now distinguish between anti-clockwise and clockwise stellar orbits with the notation $\mathrm{d}\theta = \pm v_{\rm c}/r\,\mathrm{d}t$. The anti-clockwise orbits are anti-aligned (+ sign) while the clockwise orbits are aligned (−sign). Integrating and summing the two terms, we find

$$W = -\frac{GM_{\rm bh}}{r}\,\frac{\alpha}{1 \mp \nu}\left(\sin[\frac{2\pi}{\sqrt{\mathcal{M}}} + \phi_{\rm o}] - \sin[\phi_{\rm o}]\right), \tag{17}$$

with the definitions (7) and (10) for the ratios ν and α, respectively. This equation shows that aligned (−) orbits take in more energy from the BH, while anti-aligned ones (+) see a weaker effect. The BH would therefore introduce anisotropy in an initially isotropic stellar velocity distribution function. This is not unlike the bar amplification process proposed by Lynden-Bell (1979): the angular frequency ω sets the rotation speed of a constant-magnitude quadrupole, as in a barred galaxy. However, here the perturbation to the axisymmetric galactic potential is not the two-fold symmetric $m = 2$ mode, but the $m = 0$ lopsided mode.

2.2.2 Binary BH, star cluster

The case of a circular binary BH of masses $M_{\rm bh,1}$ and $M_{\rm bh,2}$, and centred on the origin of coordinates is derived from equation (17) through a thought experiment. We imagine that the binding energy of the binary is large and so both holes revolve at the same angular frequency ω about the centre. The total contribution of the binary to W is a sum of two single circular BH orbits. The phase of the closed periodic BH orbits differs by $-\pi$ and we have in obvious notation

$$\alpha_1 M_{\rm bh,1} = \alpha_2 M_{\rm bh,2},\ \ \nu_1 = \nu_2.$$

On inspection of equation (17) and inserting $\phi_{\rm o,1} = \phi_{\rm o,2} - \pi$, it follows that the total work W vanishes for any phase angle $\phi_{\rm o}$. This will be the case also when $M_{\rm bh,1} \neq M_{\rm bh,2}$. The situation is more interesting when the BHs are unbound and so do not revolve about the centre at precisely the same frequency, giving $\nu_1 \neq \nu_2$. In that situation, the net work will not cancel, provided that

$$M_{\rm bh,1}\,\frac{\alpha_1}{1 \pm \nu_1} \neq M_{\rm bh,2}\,\frac{\alpha_2}{1 \pm \nu_2}. \tag{18}$$

The limit where $M_{\rm bh,2} \ll M_{\rm bh,1}$ reduces to the case of a single BH (the secondary) in orbit in the axisymmetric potential of the primary at rest at the origin of coordinates. The net work on the stars is once more derived from equation (17). Such a situation might occur when a swarm of intermediate-mass BHs revolve around a massive hole, presumably the result of repeated coalescence. O'Leary & Loeb (2007) have recently explored the scattering of stars in such a cluster of massive objects. Another possibility is when the intermediate-mass hole is replaced with a small cluster of stars. The impact of such a configuration on the surrounding stars would be identical to the one of the hypothesized BH on a circular orbit.

3 CASE STUDY: THE LOGARITHMIC POTENTIAL

The coupling between BH motion and orbits in the harmonic potential is indicative of trends that may develop in more realistic potentials. Here, we recast our problem in the framework of the logarithmic potential,

$$\Phi_{\rm g}(\boldsymbol{r}) = \frac{1}{2}v_{\rm o}^2 \ln\left|\frac{x^2 + y^2 + z^2 + R_{\rm c}^2}{R_{\rm c}^2}\right|, \tag{19}$$

with $v_{\rm o}$ the constant circular velocity at large distances. The radius $R_{\rm c}$ defines a volume inside which the density is nearly constant. Thus, when $r \ll R_{\rm c}$ we have once more harmonic motion of angular frequency $\omega = v_{\rm o}/R_{\rm c}$. If we let

$$u \equiv \frac{r}{R_{\rm c}}, \tag{20}$$

the volume density ρ reads

$$4\pi G\rho(u) = \nabla^2\Phi_{\rm g} = \frac{v_{\rm o}^2}{R_{\rm c}^2}\,\frac{3 + u^2}{(1 + u^2)^2} \tag{21}$$

and the integrated mass $M_{\rm g}(u)$

$$M_{\rm g}(< u) = \frac{v_{\rm o}^2 R_{\rm c}}{G}\,\frac{u^3}{u^2 + 1}. \tag{22}$$

The mass $M_{\rm g}(u \gg 1) \propto u$ diverges at large distances; however, this is not a serious flaw since we will consider only the region where $u \sim 1$. The mass $M_{\rm g}(u = 1) = v_{\rm o}^2 R_{\rm c}/2G$ fixes a scale against which to compare the BH mass $M_{\rm bh}$. Since the BH will orbit within the harmonic core, we set

$$M_{\rm bh} \equiv \tilde{m}_{\rm bh}\frac{v_{\rm o}^2 R_{\rm c}}{2G} = \tilde{m}_{\rm bh} M_{\rm g}(u = 1) \tag{23}$$

with $0 < \tilde{m}_{\rm bh} \leqslant 1$, and

$$\mathcal{M}(u) = 1 + \tilde{m}_{\rm bh}\frac{1 + u^2}{u^3}$$

bears the same meaning as before. The core radius offers a reference length to the problem. The position and velocity of the BH at any time follow from equation (5), where the amplitude is set by

fixing the dimensionless number $u_o = R_o/R_c$. Our goal is to quantify the time-evolution of a large number of orbits in the combined logarithmic and BH potentials. If we pick parameters such that

$$m_\star \ll M_{bh} < M_g(\max\{u\}),$$

then we may neglect the collective feedback of the stars on the BH and galactic potential and study only the response of individual orbits evolving in the time-dependent total potential. This approach will remain valid so long as the response of the stars is relatively modest. The time-evolution of orbits was done numerically as described below.

3.1 Equations and numerics

The energy per unit mass E_J of a star is

$$E_J = \frac{1}{2}v^2 + \Phi_g(\boldsymbol{r}) + \Phi_{bh}(\boldsymbol{r}, t) \tag{24}$$

where Φ_{bh} was defined in equation (3). We use the fact that $\dot{E}_J \neq 0$ and set $z = \dot{z} = 0$ to obtain six first-order differential equations

$$\frac{\mathrm{d}}{\mathrm{d}t}(\boldsymbol{r}, E_J, \boldsymbol{v}, \dot{E}_J) = (\boldsymbol{v}, \dot{E}_J, -\boldsymbol{\nabla}\Phi, F_J) \tag{25}$$

where the time-derivatives are computed in the usual way. For a BH orbit confined to the harmonic core, we find

$$F_J = \frac{GM_{bh}}{||\boldsymbol{\mathcal{R}}||^5} \times \{3(\dot{\boldsymbol{\mathcal{R}}} \cdot \boldsymbol{\mathcal{R}})(\boldsymbol{\mathcal{R}} \cdot \dot{\boldsymbol{R}}) + \mathcal{R}^2[\omega^2 \boldsymbol{\mathcal{R}} \cdot \boldsymbol{R} - \dot{\boldsymbol{\mathcal{R}}} \cdot \dot{\boldsymbol{R}}]\}, \tag{26}$$

where $\boldsymbol{\mathcal{R}} \equiv \boldsymbol{r} - \boldsymbol{R}$. Note that equation (26) also applies to three-dimensional motion and admits a simplification for the case of a radial BH orbit.

3.1.1 Compact kernel

Potential (3) is singular when $\boldsymbol{r} = \boldsymbol{R}$ which introduces large errors in the integration. To alleviate this, we redefine equation (3) using a compact kernel, effectively smoothing over the singularity. Let ε_{bh} be a constant length and write

$$\Phi_{bh}(\tilde{\boldsymbol{\mathcal{R}}}, t) = -\frac{GM_{bh}}{\varepsilon_{bh}}\hat{\Phi}(\tilde{\boldsymbol{\mathcal{R}}}, t), \tag{27}$$

whenever $\tilde{\mathcal{R}} = ||\boldsymbol{\mathcal{R}}||/\varepsilon_{bh} \leqslant 1$. We pick a compact kernel which minimizes force errors at $\tilde{\mathcal{R}} = 1$ (Dehnen 2003) and define

$$\hat{\Phi}(\tilde{\mathcal{R}}) = 1 + \frac{1}{2}(1 - \tilde{\mathcal{R}}^2) + \frac{3}{8}(1 - \tilde{\mathcal{R}}^2)^2. \tag{28}$$

This last equation fails when $\tilde{\mathcal{R}} > 1$; however, this is of no concern since the gradient is continuous at $\tilde{\mathcal{R}} = 1$ and matches exactly the one derived from equation (3) at that radius. Integration of equations (25) with equation (3), or equations (27) and (28), when $\tilde{\mathcal{R}} > 1$ or $\leqslant 1$, poses no particular difficulty, though equation (26) takes another form inside $\tilde{\mathcal{R}} < 1$ (see below).

3.1.2 Choice of units and integrator

For convenience, we have chosen scales for the background potential such that $G = v_o = R_c = 1$. Borrowing from the case of the MW BH, we set a kernel length $\varepsilon_{bh} = 2 \times 10^{-2}$ which will wipe out all high-deflection-angle collisions, that is, those due to orbits with little angular momentum.

We have used an explicit fourth-order time-adaptive Bulirsch–Stoer integrator taken from Press et al. (1992) for solving equation (25). We have performed a series of tests with a static potential by setting, for example, $\tilde{m}_{bh} = 1$ and $R_o = 0$ in equation (5). With these parameters $\dot{E}_J = 0$, and we checked that a precision of $1 : 10^{14}$ is maintained for a run-time of 400 units. In particular, we validated equation (28) by integrating radial stellar orbits running through the BH, both along the x-axis and y-axis. We also integrated a circular orbit at the edge of the kernel, or $\tilde{\mathcal{R}} = 1$, and found no indication of a drift in energy or any kind of random fluctuations.

The situation is less glorious when integrating with finite BH motion. To see why, let us write down F_J in equation (25) with equations (5), (27) and (28) with $\tilde{\mathcal{R}} < 1$. Some straightforward algebra yields

$$F_J = \frac{GM_{bh}}{2\varepsilon_{bh}^3} \times \{-6(\tilde{\boldsymbol{\mathcal{R}}} \cdot \dot{\boldsymbol{R}})^2 + 6(\tilde{\boldsymbol{\mathcal{R}}} \cdot \dot{\boldsymbol{r}})(\tilde{\boldsymbol{\mathcal{R}}} \cdot \dot{\boldsymbol{R}}) + (5 - 3\tilde{\mathcal{R}}^2)(\dot{R}^2 + \omega^2 \boldsymbol{\mathcal{R}} \cdot \boldsymbol{R} - \dot{\boldsymbol{r}} \cdot \dot{\boldsymbol{R}})\}. \tag{29}$$

Since the relative distance between the star and the BH is $< \varepsilon_{bh}$, we find that $F_J \sim O(1/\varepsilon_{bh}^3) \sim O(10^6)$ for the choice $\varepsilon_{bh} \sim 10^{-2}$. As such this would not be a cause for concern, however, the time-steps required to maintain an accuracy of $1 : 10^{14}$ for a typical integration time become tiny, and the computer run-time, prohibitive. We found a practical solution to this problem, by imposing that the quantity $\varepsilon_{bh}^3 F_J$ be integrated to a precision of $2 : 10^{12}$, so that F_J is known to six significant digits. Whenever this condition was not met, we only included the orbit in the analysis *up to* that point in time, after which it was ignored. This situation occurred relatively seldom, and affected some 3–4 per cent of cases at most. This was so, for example, when the initial configuration either started out with many stars on near-radial orbits and small-amplitude BH motion, or when the BH was allowed to flirt with a large number of stars by covering a distance comparable to or exceeding its radius of influence.

3.2 Initial conditions

We limit our exploration to the case of coplanar motion. The volume density (21) stretches to infinity and yields a divergent integrated mass. Since we are only interested in the central-most volume, we decided to keep only stars that remain inside a given radius. (A selection by energy E_J would be equivalent.) Our model calculation of Section 2 had shown that the response of the star to BH motion is a strong function of the ratio of their orbital periods. The orbital period of the star is proportional to $1/\sqrt{G\overline{\rho}}$, where $\overline{\rho}$ is the mean volume density inside the semimajor axis of the orbit. These two observations combined suggests that we only include orbits out to where the density varies most rapidly. We chose to truncate the system at a radius r_t such that $u_t = r_t/R_c = e \approx 2.71(8)$, close to the value $u = 2.80(7)$ at which $\mathrm{d}\ln\rho/\mathrm{d}\ln u = -2.101\ldots$ reaches a minimum. The integrated mass (22) gives $GM_g(e)/(v_o^2 R_c) \simeq 2.39(4)$. About one-quarter of the stars (21 per cent) lie inside R_c, so most stars avoid the harmonic region where the BH orbits.

Positions are attributed by the Monte Carlo method using the spherical density (21) as probability distribution and then imposing $z = 0$. The square circular velocity at each radius is

$$\left(\frac{v_c}{v_o}\right)^2 = \frac{u^2}{u^2 + 1} + \frac{\tilde{m}_{bh}}{2u} \tag{30}$$

and the sense of motion chosen randomly so that the total angular momentum of the stars is zero to within root-n noise. The energy

per unit mass may be written as

$$\frac{2E_{\rm J}}{v_{\rm o}^2} = \ln|u^2+1| + \frac{u^2}{u^2+1} - \frac{\tilde{m}_{\rm bh}}{2u}. \quad (31)$$

This expression is easily differentiated to yield an analytical form for $E'_{\rm J} = {\rm d}E_{\rm J}/{\rm d}u$ which is the density of states of stars of energy $E_{\rm J}$ at u. Since all orbits are confined to the x–y plane, the mass drawn from equation (21) within concentric annuli of radii u, $u + {\rm d}u$ is

$$\delta M_{\rm g} = 2\pi R_{\rm c}^3 \rho(u) u\,{\rm d}u \equiv f(u)\,{\rm d}u = f(u)\frac{{\rm d}E_{\rm J}}{E'_{\rm J}} \equiv f(E_{\rm J}){\rm d}E_{\rm J}$$

where the energy distribution function $f(E_{\rm J})$ is known in the parametric form

$$f(E_{\rm J}) \equiv \frac{R_{\rm c}v_{\rm o}^2}{G}\frac{u^3(3+u^2)}{\tilde{m}_{\rm bh}(u^2+1)^2 + 4u^3(u^2+2)}. \quad (32)$$

This equation shows that when $\tilde{m}_{\rm bh} = 0$ (no BH) we find $f(E_{\rm J}) \rightarrow$ constant in the limit $u \rightarrow 0$, and $f(E_{\rm J}) \propto u^3$ in the same limit when $\tilde{m}_{\rm bh} \neq 0$. Thus, the bulk of the stars avoid the central BH. Equation (32) will be helpful when assessing the noise level of the response of the stars to BH motion.

4 RESULTS

We have until now fixed the gravitational constant $G = 1$ and galactic potential velocity- and length-scale $v_{\rm o} = R_{\rm c} = 1$. The initial conditions require further that we fix the BH mass parameter $\tilde{m}_{\rm bh}$ in equation (23) and amplitude of motion, $u_{\rm o}$. The BH's radius of influence is obtained in terms of $\tilde{m}_{\rm bh}$ from equating equation (22) to equation (23). The result is graphed in Fig. 3. We use this relation to set a more stringent constraint on the motion of the BH by imposing that it orbits inside its radius of influence, an improvement on our initial ansatz that $u_{\rm o} < 1$, since equation (5) is a solution only near the origin.

4.1 Reference case, $\tilde{m}_{\rm bh} = 0.3$

We set up a reference case, labelled C3 in Table 3, which will guide us through our exploration of parameter space. Since the MW BH lies close to the Galactic Centre at a velocity $\simeq$2–4 km^{-1}, this suggests that we focus on cases where the BH remains well inside the central core. We pick a BH mass equal to 30 per cent of the core mass, $\tilde{m}_{\rm bh} = 0.3$, and set an upper limit of $u_{\rm o} = R_{\rm o}/R_{\rm c} = 0.66$ on its amplitude of motion, when it would exceed slightly its influence radius $R_{\rm bh} \simeq 0.57R_{\rm c}$ (Fig. 3).

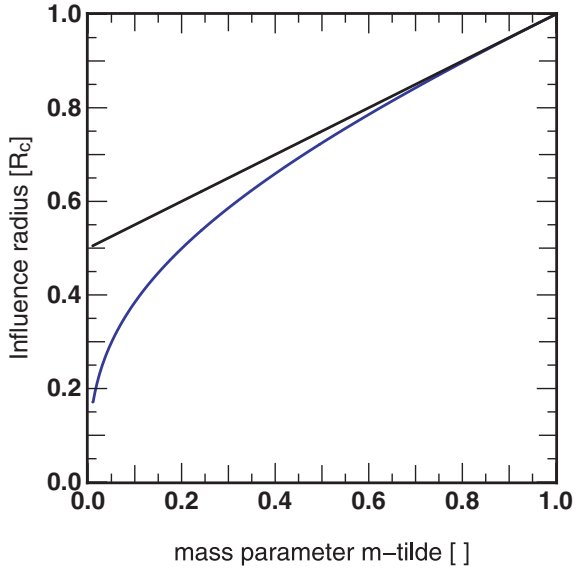

Figure 3. Influence radius $R_{\rm bh}$ as a function of the mass parameter $\tilde{m}_{\rm bh}$ defined in equation (23). In the limit $\tilde{m}_{\rm bh} \rightarrow 0$, $R_{\rm bh} \propto \tilde{m}_{\rm bh}^{1/3}$ rises rapidly, while $R_{\rm bh}(\tilde{m}_{\rm bh} \rightarrow 1) \propto \tilde{m}_{\rm bh}$; the straight line is the curve $\tilde{m}_{\rm bh}/2 + \frac{1}{2}$.

4.1.1 *Illustrative cases*

To see how orbits respond as $u_{\rm o}$ is increased from zero, we draw in Fig. 4 Poincaré sections of a single orbit for four values of $u_{\rm o}$: 0, 0.15, 0.33 and 0.66. The case of a fixed BH is shown in Fig. 4(a), when the star describes a circular orbit of radius $r = 1.78R_{\rm c}$ which is $\gtrsim 3R_{\rm bh}$. The orbital period is equal to $2\pi\, r/v_{\rm c} = 12.03$ and the integration was for a total of 200 time units (18 revolutions). The middle and right-hand panels show the orbit and the star's energy (solid curve) and distance to the BH (labelled $r_\star$, dashed curve), respectively. Fig. 4(c) illustrates the situation when the BH motion has an amplitude $R_{\rm o} = 0.33R_{\rm c} \simeq 0.58R_{\rm bh}$. The star's orbital radius now varies from a minimum of approximately $1.65R_{\rm c}$ and up to $1.85R_{\rm c}$, a gap of $\approx$10 per cent compared to the circular orbit; the same applies to the cycles seen in binding energy (right-hand panel, Fig. 4c). We note that the modulations in $E_{\rm J}$ match one to one the profile of $r_\star$, which is an indication that a strong coupling is operative even for stars orbiting well beyond the BH's radius of influence. The scatter seen in the Poincaré sections of both Fig. 4(c) and (d) confirms this view.

4.1.2 *Test of circular motion for three orbits*

The analysis of Section 2 shows that at large distances from the centre the orbit of a star will remain nearly circular. We wish to test this hypothesis against numerical integration of orbits at three different radii, for the same BH mass and amplitude of motion. Table 1 lists the parameters of the orbits along with their time-averaged energy $\langle E_{\rm J}\rangle$ and the standard deviation computed for a total of 100 time units of integration. Setting $u_{\rm o} = R_{\rm o}/R_{\rm c} \simeq 0.217$ and BH mass such that $M_{\rm bh}/M_{\rm g}(1) = \tilde{m}_{\rm bh} = 0.3$, we compute a value of $\alpha = u_{\rm o}/u$ for each orbit ranging from (roughly) 0.1 to 0.3. We evaluated the energy as a function of time from integral (9) but set in the second-order polynomial approximation (the sum of equations B2 and B3 in Appendix B). An energy $2E_{\rm J}/v_{\rm o}^2 \simeq -0.54$ corresponds to $\alpha = 1$, as shown in Fig. 2(a).

Fig. 5 shows $E_{\rm J}$ as a function of time for the three cases. Orbit #1 has the smallest value α and remains nearly circular throughout. The thick lines give the numerical solution for the same configuration but two values of $\phi_{\rm o} = 0$ (solid line) and $\phi_{\rm o} = \pi$ (dashed line). The thin lines are the analytical predictions. We find good agreement overall for the three cases. The range of $|E_{\rm J}|$ remains true to the numerical solution except for a shift out of phase as time increases. This is an indication that the precession of the star is not accurately accounted for when computing equation (15). The orbits #2 and #3 show an asymmetry between the maximum and minimum values with respect to the initial value. We see here a stronger effect in the numerical solutions than obtained from analysis (see Fig. 2a). Despite these caveats, each case depicted recovers the essential feature of a (quasi-)periodic trend in energy. Therefore, the time-averaged energy is of approximately the initial value, while the standard deviation obtained from analysis (0.016, 0.060 and 0.26, respectively for each case) is a close match to the values found from the numerical

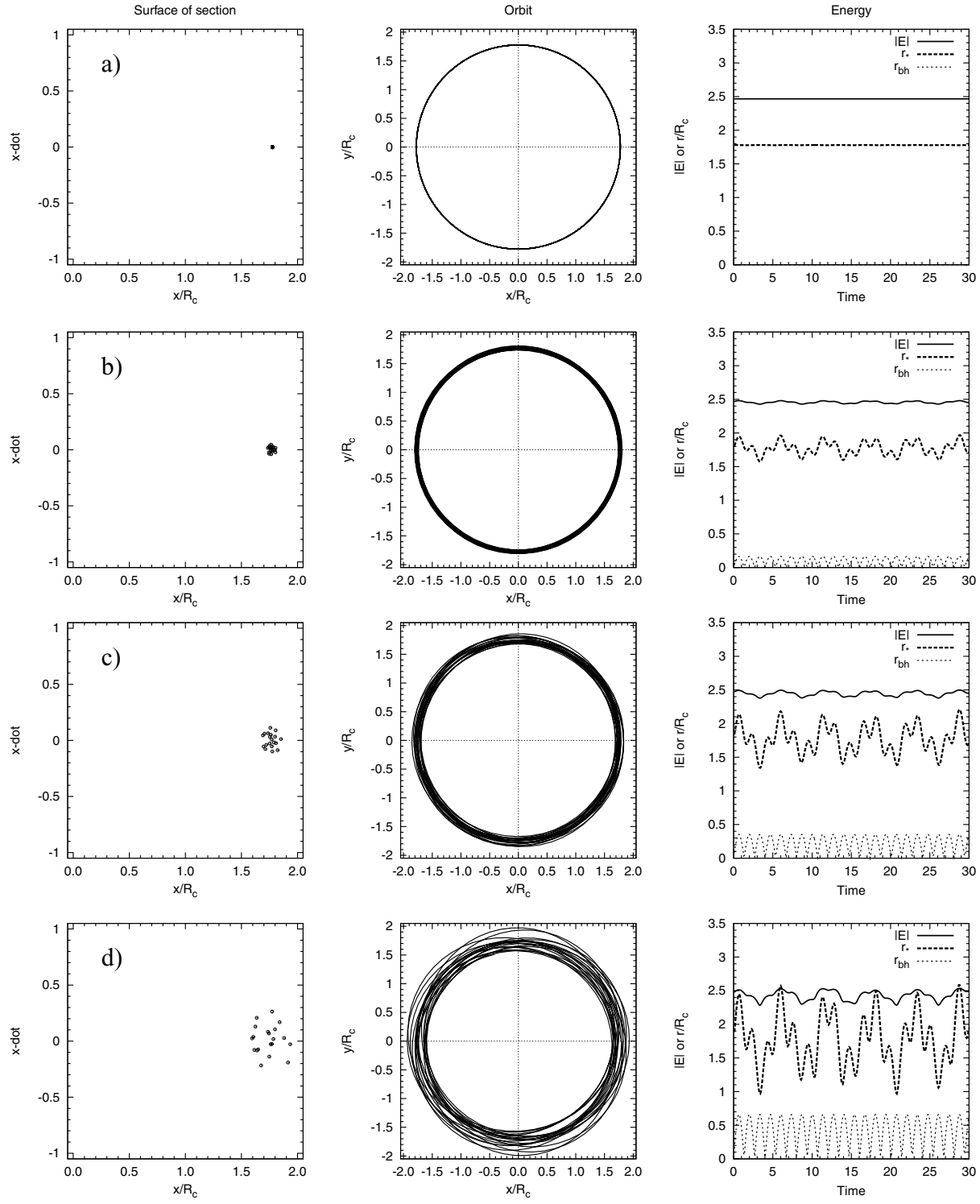

Figure 4. Poincaré section $(\dot{x}, x)$ at $y = 0$ (left-hand panels), orbit (middle panels) and radii and energy (right-hand panels) for a single stellar orbit in the logarithmic potential to which we added an $\tilde{m}_{\rm bh} = 0.3$ BH. The panels to the right-hand side display the dimensionless binding energy $E = 2E_{\rm J}/v_{\rm o}^2$ of the star (solid line) along with the distance $r_\star$ of the star to the BH (dash). Modulations in energy match one to one variations in $r_\star$. The BH orbit $r_{\rm bh}$ (dots) is also displayed for comparison. The four rows show the orbit for different values of $u_{\rm o}$: (a) 0.0, (b) 0.15, (c) 0.33 and (d) 0.66.

integrations (Table 1). The impact of BH motion on stellar orbits is not fully accounted for by analysis of restricted motion, however. A fuller account must proceed with an exploration of a large ensemble of orbits integrated numerically.

4.1.3 Distribution functions

The response of individual orbits to BH motion would leave a measurable trace only if their signal rises above the background noise of

Table 1. Parameters of selected orbits[a]. The time-averaged energy is denoted $\langle E_J \rangle$, and δE_J is the rms standard deviation.

#	u (r/R_c)	E_J ($v_o^2/2$)	$\mathcal{M}$	α	ν	$\langle E_J \rangle$ ($v_o^2/2$)	δE_J ($v_o^2/2$)
1	1.76	2.092	1.11	0.12	1.97	2.10	0.016
2	1.14	1.282	1.23	0.19	1.43	1.24	0.072
3	0.82	0.750	1.46	0.27	1.17	0.62	0.296

[a]See equations (7), (8) and (10) for definitions.

other orbits that may be otherwise affected. We sought out a relation between an unperturbed and time-independent distribution function and the noise level of a discrete realization of that function with N bodies. The reference distribution function is given by equation (32) which we discretised using 100 equal-size bins of width $2\Delta E_J/v_o^2 \simeq 0.14$. This curve is plotted as a histogram in Fig. 6. We then measured the rms differences with the analytic distribution function by drawing different orbits with N in the range 10 000–100 000. The results are shown for three values of N in Figs 6(a)–(c). We find that the rms differences drop to ∼4–5 per cent already for $N \gtrsim 40\,000$, comparable to Poisson noise (roughly $1/\sqrt{400} \simeq 5$ per cent fluctuations per bin). For completeness, we also plot the relative differences in percentage at each bin of energy on the rectangular frames below each panel. This relative energy error is dominated by low-number statistics and becomes very large when $2E_J/v_o^2 \lesssim -1$ which, for our choice of parameters, corresponds to a radius $u \simeq 0.074$ enclosing ≃0.02 per cent of the total mass (expected Poisson noise of ≈20 per cent). The error made in dropping orbits below that level of energy from our analysis is of the same order. Furthermore, stars that are close or closer to the origin would be bound to the BH and remain on high-velocity Keplerian orbits around it. This would hold true even if the BH were set in motion at a comparatively small velocity. Such orbits are not the focus of this work.

Fig. 7 compares the energy distribution function of a set of 93 617 orbits when the BH is set in motion with amplitude $u_o = 0.33$, to the initial distribution function, when the BH sits at the origin. Recall that this latter distribution would be time-independent. The orbits were all integrated for $t = 40$ units of time, which corresponds roughly to two revolutions at the edge of the system. The energy axis is once more split in 100 bins, and we find once more an rms noise level of ≈4 per cent. Let us take as one standard deviation a difference of 5 per cent with the analytic function (32). The signature of BH motion seen in Fig. 7(b) leaves four peaks of more than three standard deviations, and 10 with one or more standard deviations, all to the right-hand side of $2E_J/v_o^2 = -1$. The most significant peak

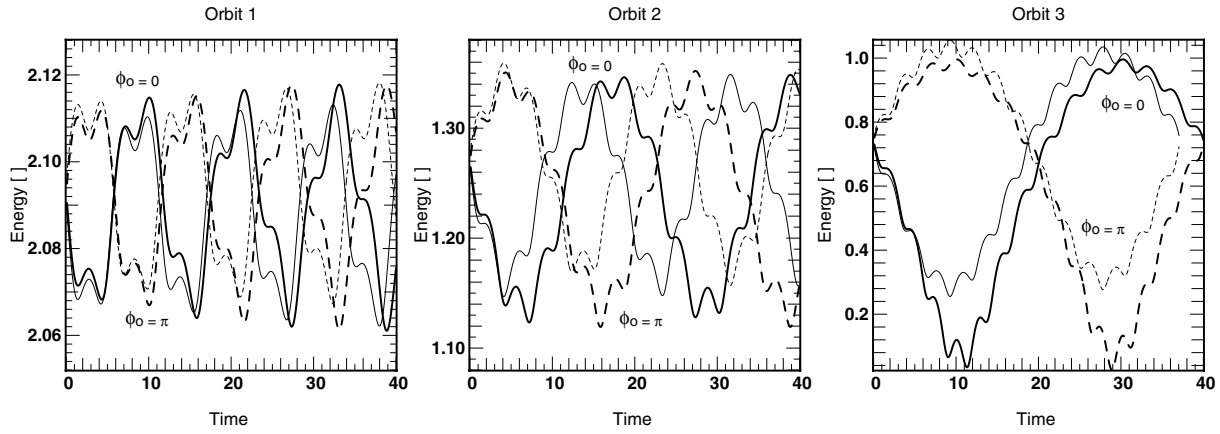

Figure 5. This graphs the energy per unit mass $2E_J/v_o^2$ as a function of time for the three orbits listed in Table 1. The thick lines are the results of numerical integration of the equations of motion; the thin curves show the result derived from equation (9) but in the second-order approximation in the Taylor development of the radical (Appendix B for details). Each type corresponds to one of two values of ϕ_o as indicated.

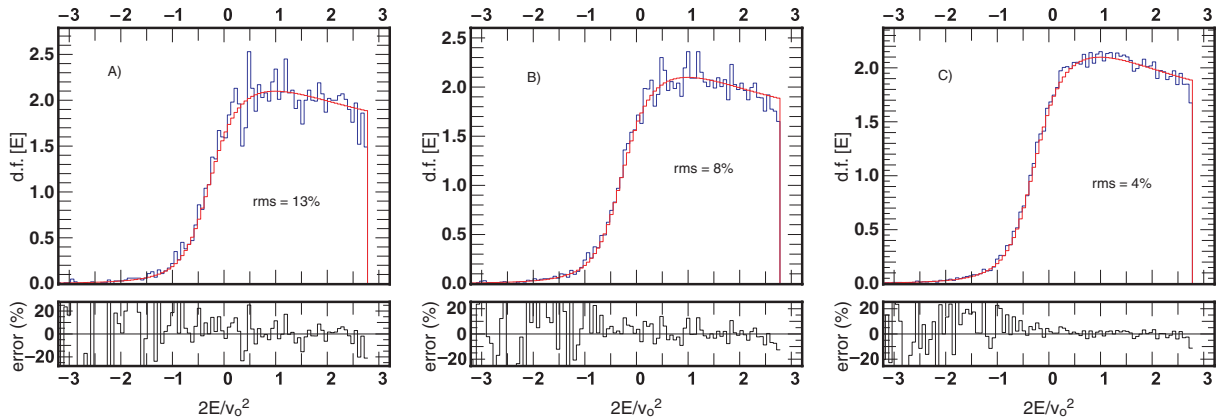

Figure 6. The energy distribution function (d.f.) for three discrete realizations with [from (a) to (c)]: $N = 10\,000$, 20 000 and 80 000 orbits. In each case, the span in energy was divided into 200 bins of equal size. The analytic curve (32) is displayed as the more regular histogram in each panel, and the rms differences given. The rectangular frames give the relative differences (in per cent) for each bin.

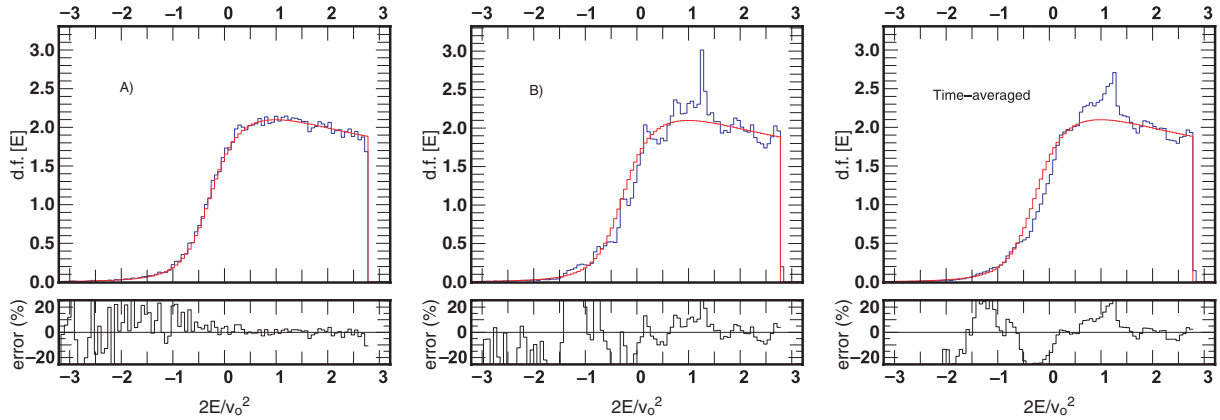

Figure 7. Energy distribution for two configurations: (a) static BH at the centre of coordinates; (b) BH on a radial orbit of amplitude $u_o = 0.33$, after 40 time-units of evolution. In both cases, the mass parameter $\tilde{m}_{bh} = 0.3$. The energy distribution function averaged over five output times is shown in the right-hand side for comparison. The smooth histogram on all three panels was constructed using equation (32).

at $2E_J/v_o^2 \simeq 1.31$ has an amplitude of +29 per cent, or five standard deviations. This corresponds to a circular orbit at radius $r = 1.169R_c$ ($= u$ since $R_c = 1$ defines one unit of length), which is approximately two times the BH radius of influence (cf. Fig. 3) and 3.57 times its amplitude of motion, R_o. This is a strong hint of energy exchange through beat frequencies, that is, resonances.

4.2 Orbital resonances

To gauge the importance of orbital resonances, we identify first the radius and energy of commensurate orbital periods. Calling $\omega_\star$ the orbital angular frequency of a star on a given orbit of energy E, we need to solve for $\nu = \omega/\omega_\star$ in

$$\nu^{-2} = \frac{1}{u^2+1} + \frac{\tilde{m}_{bh}}{2u^3} \equiv \left(\frac{m}{n}\right)^2 \qquad (33)$$

for all prime integer ratios m/n. The above equation could be set in terms of $\mathcal{M}$ defined in equation (8), as done in equation (14) in the case of a harmonic potential. Instead, we solve for E, u from equation (33), and classify the result as a Keplerian resonance when the corresponding value for $\mathcal{M} > 2$, which will always be the case when $m > n$, and a Galactic resonance for all cases where $m \leqslant n$. Table 2 lists the results for a broad range of values of m:n. Remarkably, the energy level of *Galactic* resonances matches almost exactly the apparent nodes in the energy distribution function seen in Fig. 7(b). This is in close agreement with our analysis of Section 2, when we argued that commensurate values of ν would give no net work after an integer number of revolutions. This is not the whole picture, however, since the binding energy of individual orbits is constantly changing with time, with as many stars gaining energy as those losing energy. Hence, one may think of the energy distribution function of Fig. 7(b) as a standing wave modulated by small sinusoidal modes. A clearer picture emerges once we compare Fig. 7(b) to a time-averaged distribution function for the same system. In the right-hand panel of Fig. 7, we graph the average of energy distributions functions sampled over five snapshots in the time-span of $t = 28$ to 37. This corresponds to $\omega\delta t/2\pi \approx 10/2\pi R_c/v_o \approx 2$ full BH oscillations. In total 468 115 orbits were put to contribution. Comparing this curve to the one displayed in Fig. 7(b), we find fewer peaks exceeding one standard deviation. The smoother appearance of the distribution function supports the interpretation of sine-like oscillations in Fig. 7(b) as transitory features. Thus, we expect phase-mixing to erase such features on a dynamical timescale. By contrast, the two broad peaks at $2E_J/v_o^2 \approx 1$ and -0.5 remain, their amplitude hardly dented by the time-averaging. These peaks should therefore leave observable features in kinematic and density maps.

Table 2. Orbital resonances defined in equation (33) for several values of the commensurate ratio $m:n$. Results for $m \leqslant n$ (or, $\mathcal{M} \geqslant 1$) are labelled Galactic, otherwise they are labelled Keplerian ($\mathcal{M} < 1$).

Galactic $m:n$	u	$\mathcal{M}$	$2E/v_o^2$
1:1	0.748	2.117	0.602
2:3	1.292	1.371	1.490
3:5	1.479	1.296	1.744
1:2	1.849	1.209	2.178
2:5	2.390	1.148	2.691
1:3	2.918	1.115	3.097
Keplerian $m:n$	u	$\mathcal{M}$	$2E/v_o^2$
11:10	0.663	2.482	0.443
6:5	0.598	2.904	0.317
4:3	0.532	3.556	0.187
13:9	0.489	4.179	0.101
3:2	0.471	4.508	0.064
5:3	0.427	5.556	−0.031
2:1	0.364	8.045	−0.171
5:2	0.304	12.66	−0.320
3:1	0.265	18.25	−0.433

This intuition is confirmed, at least partially, by a Poincaré section of (x, v_x) in the plane $y = 0$. In Fig. 8, we graph the surface of section of 500 orbits, each evolved for 40 time-units. The number of points varies between orbits from ∼10 and up to 200, according to the period. We observe large but localized scatter in the velocities as a function of $u_x = x/R_c$. The vertical full line at $u_x \simeq 0.3$ indicates the amplitude of motion of the BH, while the dashed lines are the locations of resonances listed in Table 2. The scatter decreases rapidly as we move to large radii. Specifically, there is a sharp drop as we reach beyond the 1 : 1 resonance, and thereafter significant scatter is centred around $u_x \approx 1.6$ and 2.5. These values of u_x corre-

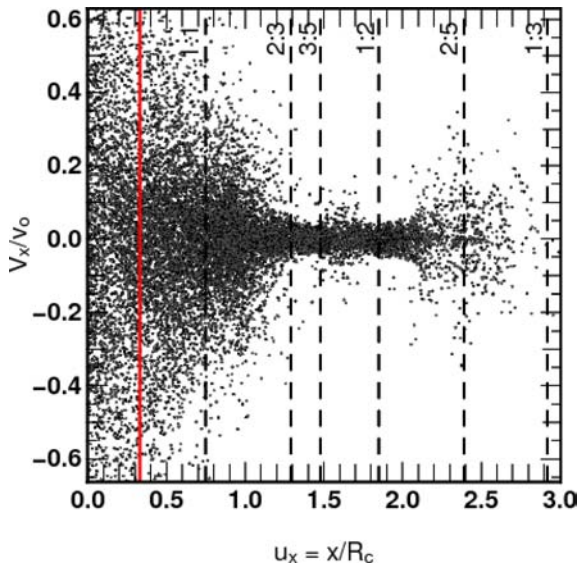

Figure 8. Surface of section in the $y = 0$ plane showing v_x in units of v_o as a function of $u_x = x/R_c$. The dashed vertical lines indicate resonances listed in Table 2. The solid line marks the BH amplitude of motion $u_o = R_o/R_c$.

spond to energies of $2E_J/v_0^2 \approx 1.9$ and 2.8, respectively, matching the features seen on the energy distribution function (cf. Fig. 7). The broad peaks seen in graphs of the energy distribution function fall inside the 1 : 1 resonance and are lost in the scatter in Fig. 8.

4.3 Surface density, velocity maps

Maps of the surface density and velocity field are of interest. The configurations are isotropic initially when the BH starts off at the centre of coordinates. At later stages, neither the density nor the velocity fields respect this initial property. We opted to map out both quantities on a uniform Cartesian grid. This has the advantage of an unbiased linear resolution over all space and is identically suited to any type of BH orbit (radial, circular or otherwise). The surface density is obtained at any time by a simple count-in-cell (CIC) technique. No smoothing or averaging of neighbouring cell has been performed. Density profiles and their significance should be interpreted with due consideration to root-n noise: a typical grid would have 30×30 mesh points, and hence a mean count per cell of at least $4 \times 10^4/900 \simeq 44$, which translates to relative fluctuations of 15 per cent. In practice, we have used of the order of 10^5 orbits, and so the noise level always falls in the range 10–15 per cent. As we will see, the density fluctuations that we measured at times exceeded 60 per cent of the reference initial profile, giving a signal-to-noise ratio (S/N) of at least 4 and perhaps as high as 7.

4.3.1 Flat-fielding the velocity map

The initial velocity (30) is known at any point in space; however, it is set in the centre-of-mass reference frame. Care must be taken when mapping out an axially symmetric velocity field on to a Cartesian grid owing to the quadratic geometry of the cells. This poses a problem around the origin of coordinates, when the radius is approximately a few grid cells only. Calling δu the grid size, we find from equation (30) an absolute error on v_c of

$$\frac{|\delta v_c|}{v_c} \leqslant \left(\frac{|\delta u|}{2u}\right)\left|\frac{2}{1+u^2} + \frac{\tilde{m}_{bh}}{2\,\max\{u,\varepsilon\}}\frac{1+u^2}{u^2}\right| \qquad (34)$$

which becomes large when $u \lesssim \delta u$. We then compute equation (34) for each orbit falling inside a given mesh and take the average square difference with the local circular velocity:

$$\frac{1}{n}\sum_{i=1}^{n}\left(\frac{||\boldsymbol{v}|| - v_c}{1+|\delta v_c|/v_c}\right)^2 \equiv \sigma^2, \qquad (35)$$

where the sum is over all n orbits inside the mesh at time t obtained by CIC. This gives a direct measure of the local dispersion as a result of BH motion, and a reference map to eliminate noise when the BH is fixed. For that case, we find using equation (35) residual errors not larger than $1 : 10^4$, or 0.01 per cent.

4.3.2 Time-sequence

We graph in Fig. 9 the time-sequence of the surface density and dispersion σ for 93 607 orbits integrated over 40 time-units. The figure shows two sets of two rows, regrouped to help match features seen in the density, to those seen in the velocity field. Initially, the orbits are isotropic and circular, which explains the two featureless frames at the top left-hand corner of Fig. 9. At subsequent times, the plots show very pronounced and fast-evolving features, both in maps of the density and in maps of the velocity. The scale of surface density was chosen to saturate at peak density enhancements of 60 per cent when compared to the initial profile. The core radius $R_c = 1$, nearly twice the BH influence radius of $\simeq 0.57R_c$, is displayed as the dashed circle. Inside and up to that radius, the mass profile shows arcs, bubbles and other transient features, all suggestive of unsteady, perhaps chaotic, orbital motion. Outside that radius, we find more steady, ring-shaped features which match the position of resonances (Table 2).

By comparison, the relative velocity dispersion peaks at $\approx$25 per cent of the local circular velocity v_c. Not surprisingly, the largest deviations in velocity nearly always coincide with the position of the BH (large dots in Fig. 9). The most-remarkable features on these frames are the large dispersions measured well outside the core radius. A particularly striking sequence runs from $t = 33$ to 37, when a large arc seems to close up on itself in the region $x \approx -1.5$, $y \simeq 0$. This large dispersion is found at a distance some five times larger than the amplitude of the BH's orbit. If we scaled these features to the MW, then an anomalous local velocity dispersion would be expected up to from 3–4 pc away from Sgr $A_\star$. In conclusion, the BH has a very strong impact on circular orbits, in terms of both spatial features and kinematics, up to approximately two to three times its radius of influence (see also Fig. 8).

4.4 Projected velocity field

The integrated line-of-sight velocity v_{1d} offers a direct way to measure the effect of BH motion. We measured v_{1d} for several configurations by applying slits of 100 mesh points running across the x- and y-axis (viewing angles of 0° and 90° to the BH orbit, respectively) covering $5R_c$ of total length. We computed both v_{1d} and the rms velocity dispersion σ_{1d} at each mesh point. The data were computed from single-time snapshots taken at $t \simeq 35$ units in each case so all orbits have made a minimum of two full revolutions. The calculation of σ_{1d} proceeds straightforwardly from (21) and (30). Inspection of several time frames, using either x or y as the

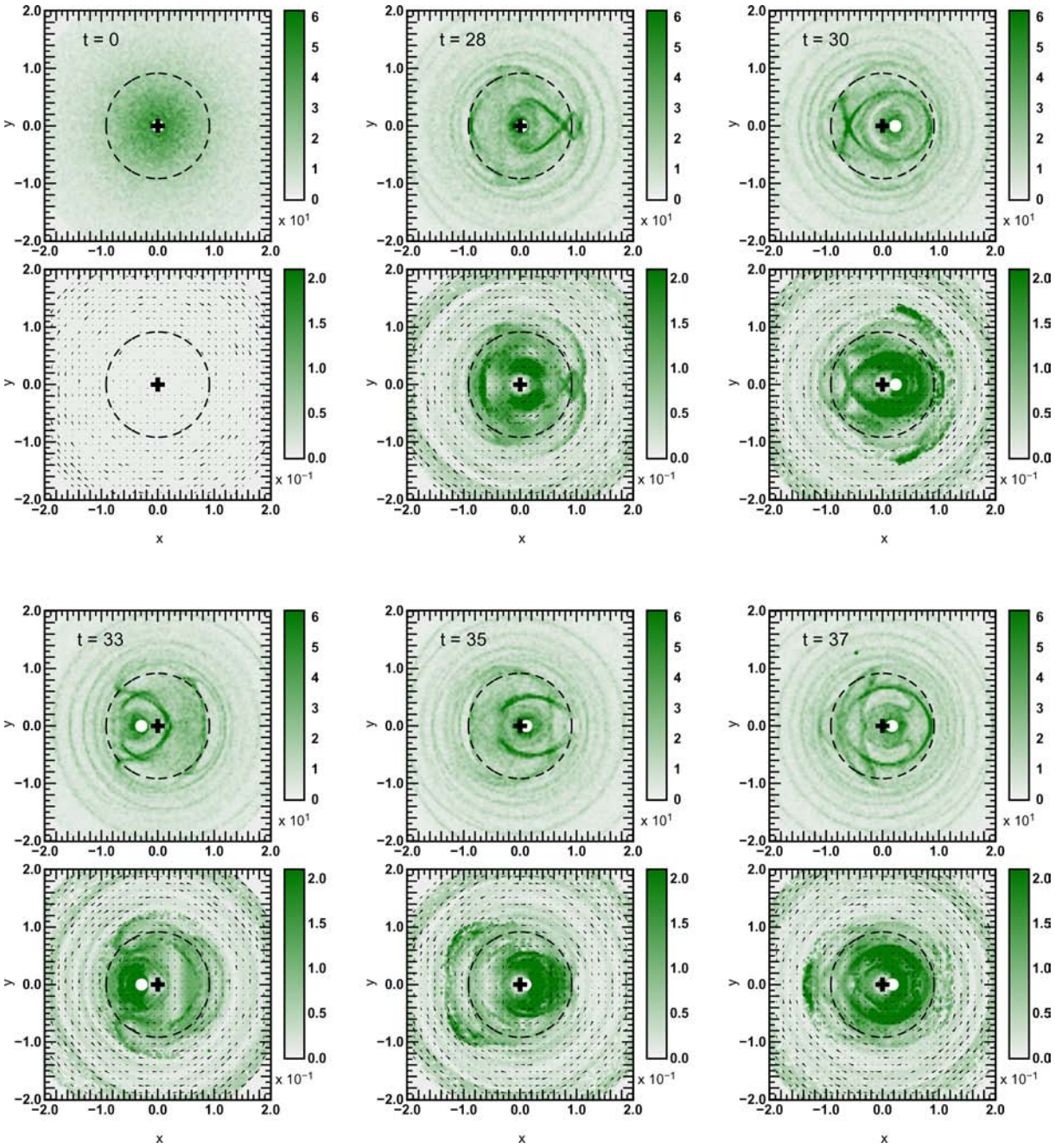

Figure 9. Time-sequence showing the surface density Σ and flat-fielded velocity dispersion σ for a system with an $\tilde{m}_{\rm bh} = 0.3$ mass BH on a radial orbit of amplitude $u_{\rm o} = 0.33\,(R_{\rm o} \approx R_{\rm c}/3)$. The frames show maps of Σ (first and third rows) and dispersion σ (second and fourth rows) at times $t = 0$, 28, 30, 33, 35 and 37 units. The BH is shown as a white circle, while the cross is the origin of coordinates. The black arrows are the local net angular momentum, which remains at the root-n level everywhere.

line-of-sight, revealed no significant deviation from the profile derived for circular motion, at any point of evolution. Fig. 10 illustrates the situation for a specific case with $\tilde{m}_{\rm bh} = u_{\rm o} = 0.3$ at four different time intervals. The dispersion derived from the isotropic stellar distribution function (dashed line) gives a good fit to the data throughout. We also looked for asymmetries in the dispersion $\sigma_{\rm 1d}$ by subtracting values on either side of the centre of the slit, pairing bins two by two, but found no significant trends (to within approximately two times the noise level; see the dotted lines in each panel). Consequently, we discarded runs of $\sigma_{\rm 1d}$ from analysis.

The situation with $v_{\rm 1d}$ is more profitable. Table 3 lists the main results for a number of configurations to which we will refer time and again from here onwards. With a total of $\simeq 10^5$ orbits put to contribution in each case, the average census per bin $\sim 10^3$ implies Poisson fluctuations ~ 3 per cent on average, for the whole slit. Because of the circular geometry of the configuration, the Poisson noise in reality is less than ~ 1 per cent inside $|u| < 1$, where the column density is highest, and ≈ 10 per cent near the end-points due to sampling effects. We found it useful to compute first averages of the absolute values of $v_{\rm 1d}$ over the entire mesh, and then over the

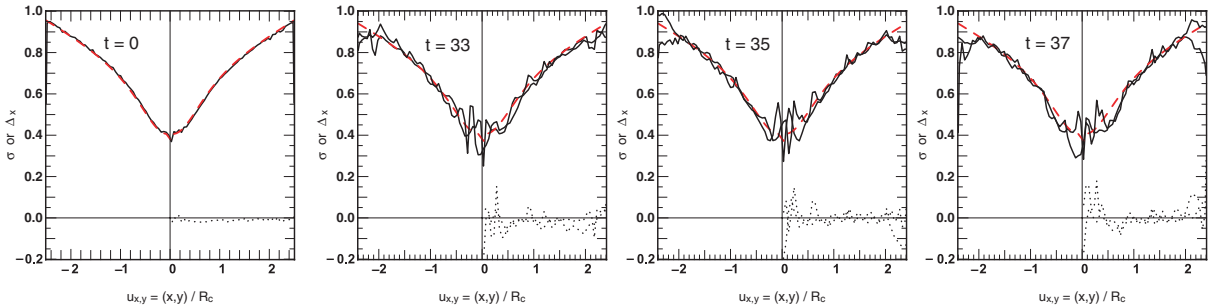

Figure 10. Time-sequence showing the line-of-sight rms velocity dispersion, σ_{1d}, for case C3 with $\tilde{m}_{bh} = 0.3 \simeq u_o$. A total of 100 bins were used for two viewing angles, down the x-axis and y-axis, in each case. At $t = 0$ (panel to the extreme left-hand side), the analytic expectation with a BH at the centre of coordinates is well recovered from 69 773 circular orbits. The dashed line shows the theoretical expectations which drop to zero at the origin (all motion is orthogonal to the line of sight). The solid line gives the dispersion recovered from summing over all orbits. The thin dotted lines are the differences about the coordinate centre $\Delta = \sigma(u) - \sigma(-u)$ for each line of sight.

Table 3. Parameters of the numerical orbit integrations and results after $t = 35$ units of evolution. The influence radius R_{bh} defined in equation (2) is given in computational units. The potential (19) is defined in units such that $G = v_o = R_c = 1$. The indices x and y refer to the position of the slit. The code names are: C = cold distribution function (circular orbits); W = warm distribution function; H = hot distribution function (see the text for details).

Name	$\tilde{m}_{bh}$	R_o (R_c)	R_{bh} (R_c)	$2\delta E/v_o^2$ ($\pm$ *per cent*)	$\overline{v_{1d}}/v_o$		rms$(\delta v_{1d})/v_o$		$\overline{v_{1d}}/v_o$		rms$(\delta v_{1d})/v_o$	
					y	x	y	x	$\lvert y\rvert < R_{bh}$	$\lvert x\rvert < R_{bh}$	$\lvert y\rvert < R_{bh}$	$\lvert x\rvert < R_{bh}$
C1[a]	0.30	0.00	0.56	0	0.026	0.028	0.028	0.036	0.005	0.005	0.004	0.004
C2	0.30	0.15	0.56	12 ± 6	0.040	0.037	0.046	0.041	0.008	0.007	0.010	0.010
C3[b]	0.30	0.33	0.56	29 ± 5	0.144	0.029	0.208	0.040	0.051	0.004	0.034	0.004
C4	0.30	0.46	0.56	37 ± 4	0.066	0.046	0.073	0.056	0.026	0.011	0.020	0.010
C5	0.30	0.65	0.56	51 ± 4	0.061	0.040	0.060	0.049	0.031	0.012	0.018	0.008
C2s[c]	0.15	0.33	0.43	24 ± 4	0.046	0.046	0.051	0.065	0.017	0.009	0.009	0.006
C3s	0.15	0.65	0.43	50 ± 4	0.054	0.031	0.062	0.031	0.013	0.012	0.012	0.007
W1	0.30	0.33	0.56	19 ± 6	0.057	0.023	0.042	0.024	0.046	0.007	0.023	0.005
W1c[d]	0.30	0.33	0.56	22 ± 4	0.053	0.039	0.046	0.039	0.038	0.029	0.022	0.022
H1	0.30	0.33	0.56	28 ± 8	0.042	0.019	0.030	0.018	0.019	0.012	0.011	0.009
W2	0.30	0.21	0.56	32 ± 5	0.060	0.021	0.041	0.020	0.024	0.014	0.017	0.011

[a] $t = 0$ data; [b] Reference case; [c] C2s (C3s) shadows C2 (C3); [d] Circular BH orbit.

region $-R_{bh} < r < +R_{bh}$ enclosed by the BH influence radius, to highlight the dynamics near the centre. Averages over mesh bins will be denoted with an overline. The analysis becomes more meaningful if we compute the rms dispersions along with the averages: we will denote these by rms$(\delta|v_{1d}|)$. To make sense of the data, it is helpful to summarize the situation of the simpler case where a BH is at rest at the centre of coordinates (case labelled C1 in Table 3). In that situation, the velocity field remains axially symmetric and no streaming motion develops. The data for the case C1 give $\overline{|v_{1s}|} = 0$ to within one Poisson standard deviation, for both the x-axis and the y-axis which are indistinguishable, as expected. In the following, we will treat the results for the C1 model as 'noise': a detectable imprint of BH motion would require an S/N of $\gtrsim 3$ (three standard deviations).

Fig. 11 graphs the line-of-sight velocity for four time-frames of the C3 configuration which has a BH mass parameter $\tilde{m}_{bh} = 0.3$ and amplitude of motion $u_o = 0.33$. The results are shown for two viewing angles in each case at times $t = 0$, 30, 33 and 35. Looking down

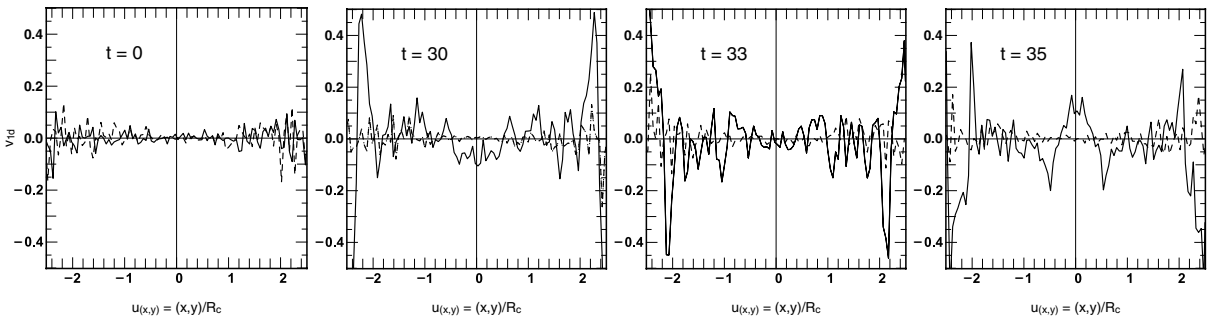

Figure 11. Time-sequence showing the line-of-sight mean velocity v_{1d} for the reference calculation with BH mass $\tilde{m}_{bh} = 0.3$ and amplitude $u_o = 0.33$. The velocity was measured when looking down the x-axis (solid line) and the y-axis (dashed line). The x-axis data show cyclical variations with a peak S/N inside $u = 1$ (or $r = R_c$).

the y-axis orthogonally to the BH orbit, we find $\overline{|v_{1d}|} = 0$ to root-n noise, a result which confirms the intuition that the y-component of the velocity field preserves the initial symmetry through the z–x plane (Fig. 11, dashed lines). A sample of these three and two more frames gave very similar results for the rms scatter rms$(\delta|v_{1d}|) \simeq 0.04$ for the whole mesh, and $\simeq 0.004$ within the influence radius.

When we switch to the x-axis line of sight, we find large time-dependent oscillations of v_{1d} of a half-period $\simeq 4$, close to half the orbital period $= 2\pi R_c/v_0 \simeq 6.3$ of the BH (Fig. 11, solid line). An inspection of Fig. 11 shows that $|v_{1d}|$ varies rapidly in space, with an rms scatter that reaches up to rms$(\delta|v_{1d}|) \approx 0.1$ (cf. case C3, x-axis data, Table 3). The time-sequence from $t = 30$ to 35 is an example of an interval during which $\overline{|v_{1d}|}$, averaged over bins inside the influence radius R_{bh}, goes from 0.051, to a minimum 0.004, and then back to 0.054. We stress that the trend with time is spatially averaged. At its maximum, the average $\overline{|v_{1d}|}$ is therefore much larger than the Poisson scatter of $\sim 5 \times 10^{-3}$ inside $|u| = R_{bh}/R_c \simeq 0.5$. If we refer to these data as noise, then the S/N when $|v_{1d}|$ goes through a maximum reaches ~ 10 near $u \approx 0$ at these times. The rms scatter of x-axis data is systematically approximately three times higher than that of y-axis data, at all times, for run C3 (Table 3). We note, however, that the scatter invariably increases with the average $\overline{|v_{1d}|}$, owing to rapid variations in space. This reduces the significance of the S/N. Furthermore, of all the configurations we have explored, the case C3 gives the highest signature of BH motion: other calculations, varying $u_o = R_o/R_c$ and/or the BH mass parameter $\tilde{m}_{bh}$ all gave a more modest global S/N of 2–3, raising to maximum values of 3–5 inside the influence radius (see e.g. runs C3–C5, Table 3).

These results highlight a close relation between the stars' angular momentum $\boldsymbol{L} = \boldsymbol{r}_\star \times \boldsymbol{v}$ and the phase of the BH orbit: the torque $\boldsymbol{\Gamma} \approx GM_{bh}/\mathcal{R}^2\,(y_\star/\mathcal{R})(x_\star - x_{bh})\hat{\boldsymbol{z}}$ (where $\mathcal{R} = ||\boldsymbol{r}_\star - \boldsymbol{R}||$ is the distance between the star and the BH) will be positive for half the stars inside a given mesh centred on $y_\star$. The torque will boost $||\boldsymbol{L}||$ when $\boldsymbol{\Gamma}\cdot\boldsymbol{L} > 0$ (otherwise the torque will oppose a star's momentum, and decrease its magnitude). This argument may be the main reason for the cyclic fluctuations seen in Fig. 11 when the line-of-sight velocity does not integrate to zero.

The impact of BH motion on the distribution of angular momentum $L = ||\boldsymbol{L}||$ appears clearly on a graph of the momentum distribution function. The top left-hand panel in Fig. 12 (labelled 'cold') shows the distribution function at time $t = 37$ for the reference calculation, compared to the initial profiling (thin dashed line). The angular momenta are distributed in a highly symmetrical fashion about the $L = 0$ axis. Each feature marking a departure from the initial distribution is matched pair-wise for the same value of $|L|$. Thus, the sum of all stellar momenta remains constant. Fig. 12 (top, left-hand panel) illustrates the role of the BH acting as a catalyst to transfer angular momentum to the stars.

4.5 Exploring different configurations

4.5.1 Changing the velocity field

Our choice of circular orbits has some bearing on the outcome of the calculations. In this section, we assess to what extent features seen in Fig. 9 are specific to our choice of initial conditions.

We first took the same set of orbits but modified initial velocities by ± 10 per cent in magnitude, so that the orbits were no longer circular initially. This exercise produced similar features in the maps of density and velocity to that for the reference set-up, a hint that the initial response of the stars, and the general features, is not sensitive to imposing strict circular motion to the initial conditions (see also Section 4.1.2). We then toyed with the idea of computing a velocity field consistent with the logarithmic potential based on moments of the Boltzmann equations (e.g. Binney & Tremaine 1987). Doing so, however, would have meant introducing a new energy distribution function and comparisons with the case of circular orbits become more difficult. Instead, we opted to keep the same energy distribution function and to change the velocity field by re-orienting the velocity vectors randomly inside some angle chosen in the interval $\pm\theta$; here $\theta = 0$ gives the original distribution function with all orbits circular. Two new configurations were set up, one with $\theta = \pi/4$ (giving a cone of opening angle 45°), which we label *warm*, and a second with $\theta = \pi$ (fully random in azimuth), which we label *hot*. The distributions were otherwise unchanged from the reference model C3. The full list of model parameters is given in Table 3.

The results are summed up graphically in Fig. 12. The top three rows show the angular momentum distribution function (left-hand panels), the surface density (middle panels) and line-of-sight velocity v_{1d} for two projection axes (right-hand panels) in turn for the 'cold' configuration of circular orbits, the 'warm' and 'hot' initial conditions. All data shown in the figure were taken at time $t = 37$ so the BH assumes the same position and velocity in each case. The rings seen in the surface density map of the cold run outside $r = R_c$ (shown as a dashed circle) have disappeared, and only the strongest feature inside R_c remains visible for warm and hot initial conditions. Thus, the filamentary structures seen in Fig. 9 are attributable to the strong response from circular and near-circular orbits. These would make up a small fraction of warm and hot distributions. In these two cases, the number of low-L orbits is higher and more stars visit the central region on eccentric orbits. These scatter off the BH and acquire large angular momenta, a feature which can be measured up from the swelling of the momentum distribution function for large $|L|$ and the depletion of the distribution function around $L = 0$ (Fig. 12, left-hand panels, second and third rows). The BH motion has $R_o = 0.15R_c$, and a radius of influence $R_{bh} \simeq 0.5R_c$. Therefore, all stars with an initial (specific) angular momentum lower than $r \times v \approx 0.52R_c v_o$ would come within a distance of $\lesssim R_{bh}$ of the BH in one revolution.[3] Fig. 12 shows this estimate in good agreement with the numerical computations. A fraction of stars of about 12 per cent are affected in this way in the 'warm' calculation, but close to 25 per cent in the 'hot' run, when circular orbits have all but been wiped out.

Although details of the density map and angular momentum profiles are much affected in the new configurations, compared to the reference 'cold' one, the same does not apply to the line-of-sight average velocity, v_{1d}. The response of stars for both 'warm' and 'hot' computations shows a distinct signature of BH motion in the sense that once again v_{1d} fluctuates significantly more when measured down the axis parallel to the BH's orbit. The averaged scatter in both the cases compares well with the data for the cold configuration of circular motion, at least in the interval from $u = 0$ to $|u| = 1$, or roughly two times the BH radius of influence (Fig. 12 and Table 3). In conclusion, the BH motion still imprints the kinematics of both warm and hot configurations, albeit to a lesser degree than for the case when stars are on circular orbits.

[3] We have set $r = R_{bh} + R_o$, that is, $u = 0.65$; $v(u) \approx 0.73$ from equation (30).

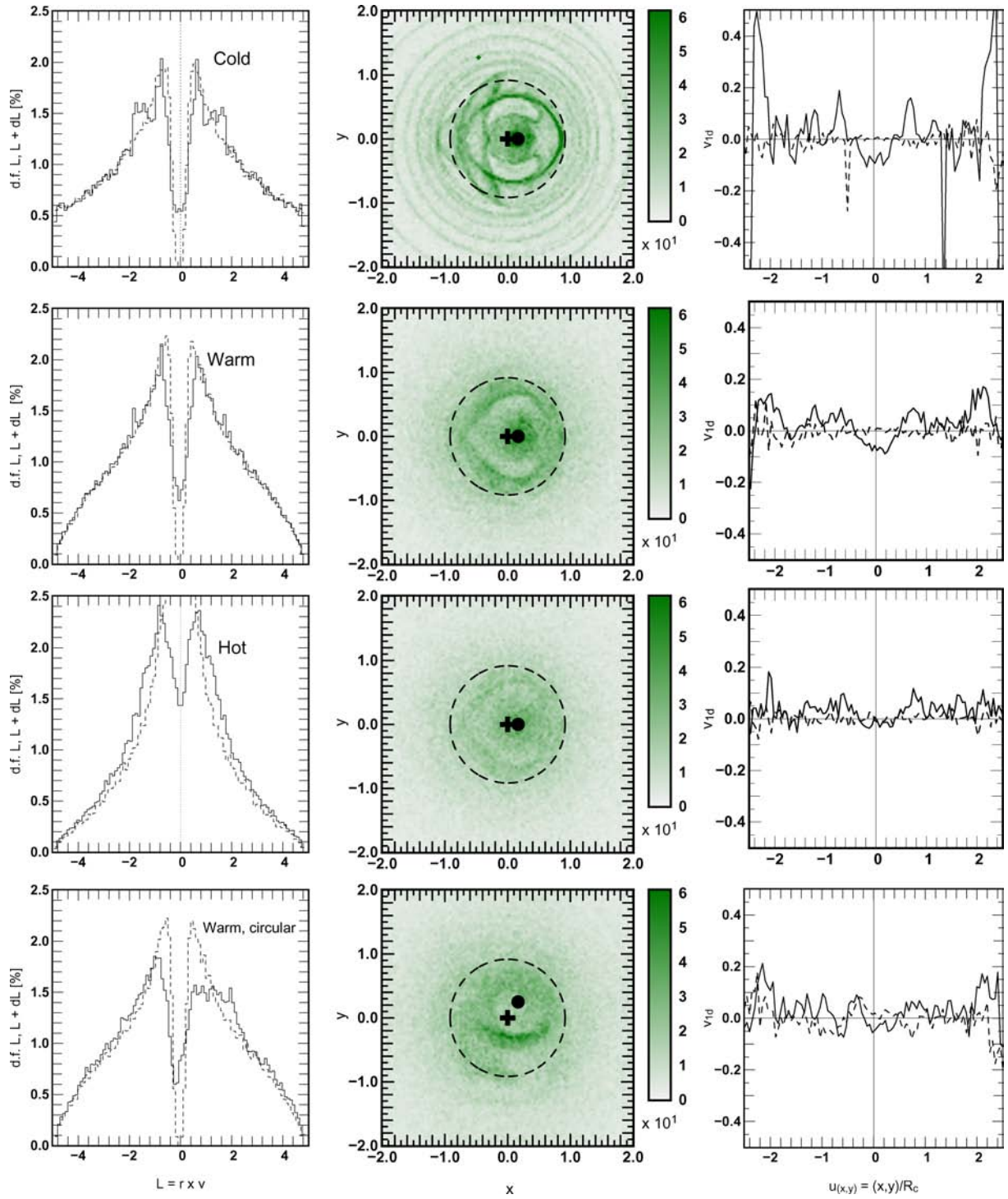

Figure 12. This graphs from the left-hand to right-hand panel: the angular momentum distribution, the surface density, and the line-of-sight velocity for four models. The top row gives the results for the reference C3 calculation; the second row is the 'warm' W1 calculation; and the third row is the case H1 of a 'hot' distribution (see Table 3 and Section 4.5 for details). All quantities were analysed after $t = 37$ time-units of integration; the BH is shown here as a black circle in the middle frames. A minimum of 93 000 orbits were used to sample each of the parameters. The row at the bottom is run W1c of a BH set on a circular orbit. Note the strong $m = 0$ mode on the map of the surface density.

4.5.2 Changing the BH parameters: scaling

Equations (13), (22) and (23) may be combined to give a proportionality relation between the work W and BH amplitude of motion and mass function $\mathcal{M}$. Keeping only the radius-dependent terms, we find

$$W \propto \frac{u_o}{u^2}\left[\tilde{m}_{bh} + \frac{u^3}{u^2+1}\right] \tag{36}$$

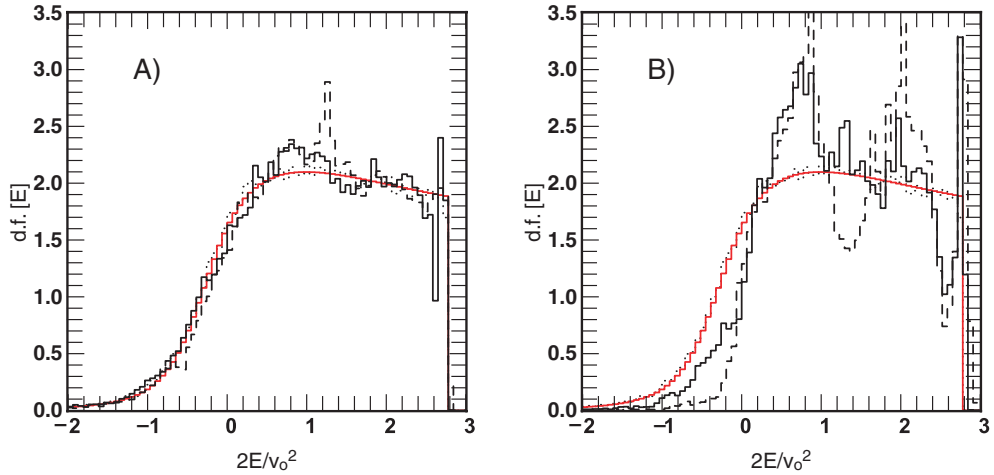

Figure 13. This graphs the energy distribution for four values of the BH's amplitude of motion $u_o = R_o/R_c$. The dimensionless mass parameter $\tilde{m}_{bh} = 0.3$ in all the cases. In panel (a) we plot two solutions with $u_o = 0.07$ (solid line) and 0.15 (dashed line); in panel (b) we set $u_o = 0.21$ (solid line) and 0.30 (dashed line). The smooth histogram is the analytic solution (28). The dots show a discrete realization with 69 977 orbits and $u_o = 0$ (axially symmetric potential). The energy $2\,E_J/v_o^2 \simeq -0.54$ corresponds to $\alpha = u_o/u = 1$.

so that the ratio $W/(u_o\tilde{m}_{bh})$ is roughly homogeneous in $1/u^2$ whenever $u^3 \ll 1$. This limit would allow to retrieve a scaled version of any calculation following a redefinition of the BH mass and/or amplitude of motion by a suitable rescaling of the lengths. However, the limit $u \ll 1$ implies that the orbit is well inside the BH radius of influence. Only a very small fraction of orbits will be found there. Nevertheless, equation (36) suggests that two configurations with $u_o\tilde{m}_{bh}$ kept constant would yield a similar net work W on some orbits and so possibly the same or comparable imprint on the stellar energy distribution function.

We investigated this with two configurations, C2s and C3s, tailored to shadow runs C2 and C3 (cf. Table 3). The two 'shadow' runs both had a BH mass equal to half that of C2 and C3, however, twice the amplitude of motion u_o. Table 3 lists the rms deviations of the energy distribution function compared to the analytic curve (32). The impact on the energy distribution function is clearly stronger for the large-amplitude BH runs. The energy deviations of 24 per cent are nearly as large for an $\tilde{m}_{bh} = u_o = 0.15$ configuration as those obtained with the same configuration but with $\tilde{m}_{bh} = 0.30$, for which we found 29 per cent deviations on the mean. In practice, the energy fluctuations scale almost linearly with the BH's orbital radius u_o, a conclusion reached by comparing the results for cases C1 to C5. As argued in the preceding paragraph, the amplitude of the response of the stars appears robust to details of the velocity field, as seen when comparing 'warm' or 'hot' stellar velocity fields (W1, H1 and W2). A configuration with a BH set on a circular orbit did not produce significantly different results compared to similar configurations with the same mass and amplitude u_o (case W1c, Table 3). Taken together, these results highlight the importance of the BH effective orbital cross-section $\propto u_o^2$ in transferring binding energy to the stars.

5 SUMMARY AND FURTHER APPLICATIONS

Oscillations of a massive BH about the centre of a host galaxy leave a signature on the kinematics of surrounding stars. We showed from an analytic harmonic potential model that stars on circular orbits lose or gain energy according to the relative phase between their and the BH's orbit: for an evenly sampled distribution function, half of the stars gain energy, while the other half lose energy. The BH plays the role of a catalyst by allowing energy exchange between the stars.

We explored a range of orbits with BH and stars in a logarithmic potential with a Bulirsch–Stoer numerical integration scheme (Press et al. 1992) using of the order of 10^5 orbits. The feedback of stars on the BH orbit was neglected, an approach motivated by the large BH to stellar mass ratio. With stars set on circular orbits, we found a strong response to BH motion, at distances ranging up to three times the BH's radius of influence (see Figs 4 and 9). Such a strong response was also seen in perturbed circular orbits, with velocity perturbations in the range ± 10 per cent. We quantified the impact of BH motion on the stars' energy distribution function. We measured rms deviations growing linearly with the amplitude of motion, $u_o = R_o/R_c$, where R_c is the core radius of the logarithmic potentials. We obtained a significant response (S/N > 4) even for modest amplitudes of $\sim R_{bh}/3$, where R_{bh} is the BH's radius of influence (cf. equation 2 and Table 3). Worried that these results concerned circular or near-circular orbits only, we reset the velocity field ('warm' and 'hot' configurations, see Section 4) but kept the original energy distribution function unchanged. This resulted in washed-out features in maps of the surface density and velocity dispersion (see Fig. 12) but left a signature on the energy distribution function of the same magnitude, with once again the BH amplitude of motion the main agent responsible for re-shaping the energy distribution function (Table 3). An analysis of the angular momentum distribution function showed that non-circular orbits visit the centre more frequently and couple more strongly with the BH at some point on their orbit. Thus, although the energy-exchange mechanism identified for circular orbits plays a secondary role in systems with warm and hot velocity fields, the BH motion still induced strong anisotropy. This was most clearly seen when profiling the net line-of-sight velocity v_{1d} resulting from two different projection angles (see Fig. 12, right-hand panels). Any level of anisotropy is attributable to the motion of the BH, since a static hole would have left the initial isotropic distribution function unchanged.

5.1 Comparison with Milky Way data

The largest values of integrated line-of-sight velocity v_{1d} were obtained from a viewing angle parallel to the motion of the BH (here, the x-axis, with the slit positioned along the y-axis, see Table 3). The most-extreme case C3 sets useful upper limits on the strength of streaming velocities sparked by BH motion. Contrasting the maximum values of v_{1d} read off Fig. 11 inside $|u_y| = 1$, to the rms velocity dispersion σ_{1d} taken from Fig. 10 at the same radial bin, we find a ratio of $v_{1d}/\sigma_{1d} \approx 0.1/0.4 \approx 25$ per cent . This gives an estimate of the maximum magnitude of streaming motion on a scale of the BH's radius of influence (see Figs 11 and 12). A more conservative estimate would take the average of $\overline{v_{1d}}$ inside $|u_y| < 1$, where Poisson statistics gives much reduced noise: we now find $\overline{v_{1d}}/\sigma_{1d} \approx 0.051/0.4 \approx 13$ per cent. Applying these two estimates to MW data, where the central velocity dispersion rises to $\sim$180 km^{-1} inside 1 pc of Sgr A$_\star$ (Genzel et al. 1996), we obtain streaming velocities in the range $\sim$23–40 km^{-1}, a rough match to the values reported recently by Reid et al. (2007). However, case C3 had a ratio $R_o/R_{bh} = 0.33/0.56 \approx 0.6$ far exceeding the value allowed on observational ground. The MW surface density profile shows a break at radius $r_{br} \sim 0.2$ pc (Schödel et al. 2007). Inside r_{br}, the volume density is fitted with a power-law index $\gamma \simeq 1.2$ which falls outside the range 3/2–7/4 of the Bahcall–Wolf solution. BH motion of an amplitude $R_o \sim r_{br}$ might cause such a break; however, the radius of influence $R_{bh} \sim 1$ pc implies a ratio $R_o/R_{bh} \lesssim 0.2$. The ratio $r_{br}/R_{bh} \sim 0.2$ compares well with the value $\approx$0.26 of run C2 (Table 3). Repeating the steps outlined above for run C3, we measure for that case a ratio $\overline{v_{1d}}/\sigma_{1d}$ in the range 2–10 per cent, which would translate to a streaming velocity ranging from 3.6 to 18 km s^{-1}, a much tighter constraint than before. These values are at best indicative since the calculations presented here did not aim to model the dynamics of the MW centre in all its complexity. Nevertheless, their outcome suggests that past and ongoing BH motion may yet leave an imprint in the form of streaming motion out to $\sim$1 pc detectable by km s^{-1} precision spectroscopic surveys.

5.2 Circular BH orbit

We were worried that a BH set on a radial orbit might trigger only a subset of resonant modes from the stars, in contrast to the more probable situation where the BH's orbit has a finite angular momentum. We recall the analysis of Section 2.2, where the response from the stars was shown to be stronger for aligned orbital angular momenta. To test this idea, we re-ran the 'warm' W1 calculation with the BH now set on an anti-clockwise circular path at a radius $u_o = R_o/R_c = 0.33$, or roughly half its radius of influence (cf. W1c, Table 3). As the BH orbits the centre, an $m = 0$ density mode develops which shows up as a trailing arm in Fig. 12 (bottom row, middle panel). The arm stretches radially from one to approximately two times R_{bh}. Its integrated mass $\simeq$40 per cent the BH's mass, and so if the gravity of the arm were taken into account, the torque that this would produce would modify the BH's orbit significantly, an effect which was neglected here. The averaged line-of-sight velocity of the stars, on the other hand, showed spatial variations of the same amplitude as in the other cases with a strictly radial BH orbit of a similar amplitude. This result comforts the thought that BH motion may yet give rise to an observable kinematic signature (especially in the profile of the averaged line-of-sight velocity v_{1d}), regardless of the precise parameters of its orbit.

5.3 Three-dimensional effects

The results of Sections 3 and 4 are limited in scope in two important ways. First, we have considered only coplanar orbital motion. Secondly, the analysis is based on a result obtained for strictly circular orbits, both conditions never fully met in realistic situations. It is therefore unclear whether the results can be exported to three-dimensional configurations.

To explore this, consider once again the three stars of Table 1. The stars will explore three-dimensional space if we rotate their initial position vector by an angle $= \vartheta$ about the y-axis, but keep the BH orbit unchanged (recall that all three begin their career on the x-axis when $\vartheta = 0$). Doing so ensures that the impact on the evolution of, for example, the orbital energy of the stars will be reduced to a minimum, since the length $||\boldsymbol{R} - \boldsymbol{r}||$ will take larger values on average than for coplanar motion.

A rough calculation helps to contrast coplanar to three-dimensional orbits. Let $\vartheta = \pi/2$ rad so $\boldsymbol{R}$ and $\boldsymbol{r}$ are now orthogonal. In that case, Φ_{bh} in equation (3) assumes an absolute minimum of $-GM_{bh}/r$, when the BH is at the centre of coordinates, and a maximum of $-GM_{bh}/\sqrt{r^2 + R_o^2}$. When moving in and out of the orbital plane of the star, the BH will exert a force perpendicular to it, and drag the star along with it. Periodic variations in the force imply $\langle \delta v_\perp \rangle = 0$ on average but $\langle (\delta v_\perp)^2 \rangle$ would match the difference in potential energy,

$$\frac{1}{2}\left\langle (\delta v_\perp)^2 \right\rangle \sim \frac{GM_{bh}}{r}\left(1 - \frac{1}{\sqrt{1+\alpha^2}}\right) \approx \frac{GM_{bh}}{r}\frac{\alpha^2}{2}$$

where $\alpha = R_o/r$ as before, and we have assumed efficient phase-mixing. For instance, in the case of orbit #3, the above estimate would give (for one full cycle) $\frac{1}{2}\langle (\delta v_\perp)^2 \rangle \sim 0.03$. Thus, contrary to the case of coplanar motion, where E_J was shown to oscillate about its initial value, in the polar orbit configuration the star would receive kinetic energy from the BH. This, then, would imply a net shift in the mean orbital energy of the star.

To validate this intuitive result, we repeated our exercise of Section 4.1.2 of computing the mean orbital energy, along with the standard deviation, for 16 values of ϑ at equal intervals in the range $[0, \pi]$. The orbits were evolved for a total of 100 time-units, for two values of the phase angle $\phi_o = 0$ and π. The results are plotted in Fig. 14. The curves of averaged energy for the most-distant orbit #1 show virtually no change with ϑ (top curves, Fig. 14a). In the case of orbits closer to the origin, orbits #2 and #3, we find an ever more significant rise in energy as we shift from a coplanar to a polar orbit ($\vartheta = \pi/2$). This is at first sight confirmation of our intuition of the transfer of kinetic energy sketched in the preceding paragraph, but note that our estimate is too low by a multiplicative factor of 3–4. Orbits closer to the centre suffer relatively stronger perturbations for any value of ϑ and, as a consequence of large time-dependent torques, their orbital plane precesses more rapidly. A three-dimensional rendering of orbit #3 confirms this. The net increase in mean energy might therefore be attributed to motion out of the initial orbital plane together with continued re-alignment of that plane.

Fig. 14(b) graphs the rms standard deviation of the energy as a function of ϑ. The closest orbit to the centre, orbit #3, sees the largest variations in mean energy and also in rms deviations. The rms deviation was shown to stem from periodic oscillations of the energy over time (Fig. 5). For coplanar motion, the amplitude of these oscillations is $O(\alpha)$ (recall equations 9 and B2), while for polar orbits we find $O(\alpha^2)$. Thus, the rms deviation drops systematically as ϑ increases; in the case of orbit #3, from $\simeq$0.15 ($\vartheta = 0$)

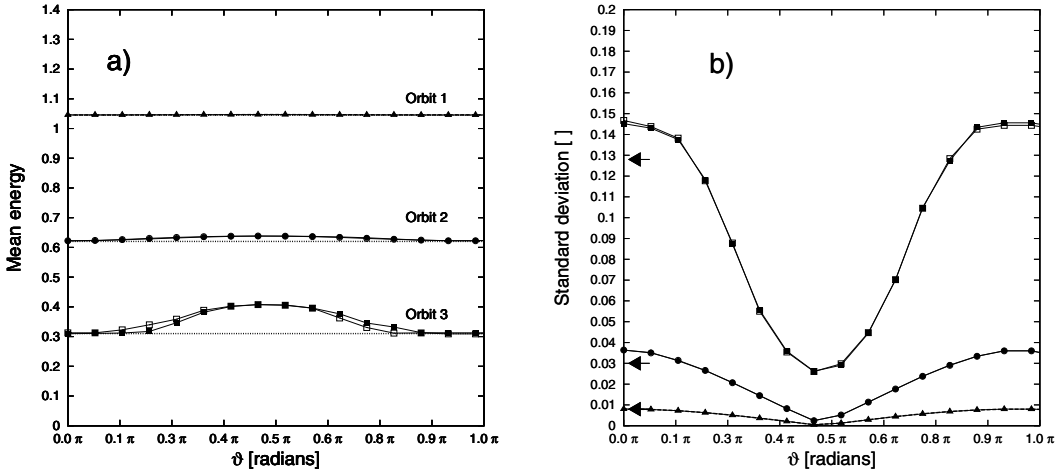

Figure 14. (a) Time-averaged energy of the three orbits listed in Table 1 as a function of the rotation angle ϑ about the y-axis. Open symbols: results for $\phi_o = 0$; filled symbols: $\phi_o = \pi$. (b) The rms standard deviation about the mean for the same orbits. Symbols are identical on both panels. The arrows indicate the values derived from analysis when $\vartheta = 0$.

to $\sim$0.04 for a polar orbital plane (Fig. 14b): the ratio of these two values is $\sim 0.3 \simeq \alpha$, that is, of the same order as the ratio of the respective values of δE for the two configurations. The same applies to orbits #2 and #1. Consequently, there exists a strong relation between the response of a star to BH motion, and the orientation in space of their respective orbital planes. However, Fig. 14 shows that both the mean energy and the rms deviation vary little as the orbital plane is shifted, from $\vartheta = 0$ up to $\vartheta \approx \pi/5$. This gives confidence that the analysis for strictly coplanar motion may apply to some $\approx$30 per cent of three-dimensional orbital configurations.

6 CONCLUSIONS AND FUTURE WORK

The imprint of BH motion on the stellar kinematics is in direct relation to the stars' angular momentum distribution function. Stars on low angular momentum orbit likely will collide with the BH, while those of large momenta experience strong beat-frequency resonances (when the BH's orbit is either radial or circular). The combined effect left the velocity field significantly anisotropic with a ratio of averaged line-of-sight velocity v_{1d} to rms dispersion reaching $\sim$13 per cent according to the BH mass and amplitude of motion (we found values in the range of 2 per cent and as high as 25 per cent, cf. Section 4.4). Because analysis suggests that the BH orbital energy is preserved to good approximation, while that of the stars varies in time, we say that the BH is a catalyst for evolution of the stellar energy distribution function.

The two-dimensional modelling done in this paper is a first attempt at isolating the generic features of a time-evolving dense nucleus with BH motion. The quantitative outcome of the calculations would be improved in a study of a family of anisotropic distribution functions, such as, for example, the Osipkov–Merritt distribution function $f(E - L^2/r_a^2)$ (Binney & Tremaine 1987, section 4.4.4), using self-consistent three-dimensional integrators. We have shown that when stars are on circular or near-circular orbits, the resonances induced by the BH likely will lead to self-gravitating substructures inside a volume of a few times R_{bh} in diameter. Such a study carried out with an N-body technique is possible, provided that collisional physics around the BH is well resolved (Preto et al. 2004). Merritt (2005) and Merritt et al. (2007) have shown that repeated collisions with stars inside $\sim R_{bh}/2$ lead to random walk and an effective 'Brownian' velocity transferred to the BH. If the random walk was of amplitude $R_{bh}/2$, this would equally imprint the kinetic motion of stars outside $\sim R_{bh}$, as we have seen, through the catalytic process that we have outlined.

We have neglected the orbital evolution of the BH. In reality, the stars inside the BH's radius of influence R_{bh} would take away energy and lead to it sinking to the centre through dynamical friction. This does not invalidate the impact of BH motion on the stellar kinematics because (i) this signature is manifested well outside $\sim 2R_{bh}$; and (ii) dynamical friction will be effective on a time-scale of approximately few orbital revolutions. Recall that the effect discussed here is effective over a single BH period.

BH orbital evolution would bring a higher degree of realism and a more fiducial comparison to observational data. We examined the case of a BH on a circular orbit which gave rise to an $m = 0$ density wave, spanning a mass of $\sim$40 per cent the mass of the BH. The gravitational torque of the wave would rapidly brake the BH, which would sink towards the centre and lock many stars along with it. If the wave were unstable to collapsing on itself and form a bound object, a double nucleus would form. The separation between the two nuclei would be $\sim 2R_{bh}$ or larger, as deduced from the density map in Fig. 12 (bottom panels). On the contrary, if the tidal field of the BH were too strong, the wave would instead merge with the BH. This would leave the BH near the Galactic Centre surrounded by a pool of stars on eccentric orbits. Tremaine (1995) has argued that the double nucleus of M31 (Lauer et al. 1993) may be such a case of an off-centre supermassive BH surrounded by a stretched Keplerian disc of size $\sim R_{bh}/2$ (0.5 arcsec separation at 800 pc, with $M_{bh} \simeq 8 \times 10^7\,\mathrm{M}_\odot$). Our calculations did not include self-gravity, and hence the fate of the $m = 0$ density wave seen in Fig. 12 remains undetermined. (See also Peiris & Tremaine 2003; Salow & Statler 2001; Bender et al. 2005 for further data on M31.) Other double or multiple nuclei detected in external galaxies (e.g. NGC 4486B and NGC 4382, Lauer et al. 1996, 2005; the Virgo Cluster dwarf VCC 128, Debattista et al. 2006) are prime examples of the strong orbital coupling of stars with a supermassive BH and its influence on the small-scale morphology of a galaxy. New data may reveal cases where double-nuclei galaxies result from the orbital coupling we have discussed here. For the MW, current and future high-precision astrometric missions, such as *RAVE* [accuracy of $\sim$1 km s^{-1} out to

8 kpc at a magnitude limit of ∼13 (*I*-band)] or *GAIA* (launch date 2011) should pick up any systematic trends in stellar kinematics.

ACKNOWLEDGMENTS

It is a pleasure to acknowledge the referee, L. Subr, for a constructive report and for alerting us to equation (A3). Much of the work of Section 5.3 was carried out by S. Richard in Strasbourg during a summer assistantship. We would like to thank T. Lauer and V. Debattista for comments on an earlier version of this paper. CMB was awarded a travel grant from the Indo-French Astronomy Network which made possible a visit to IUCAA in January 2007. Our warm thanks to IFAN's A. K. Kembhavi and A. Lecavelier des Etangs for support.

REFERENCES

Backer D. C., Sramek R. A., 1999, ApJ, 524, 805
Bahcall J. N., Wolf R. A., 1977, ApJ, 216, 883
Begelman M. C., Blandford R. D., Rees M. J., 1984, Rev. Modern Phys., 56, 255
Bender R. et al., 2005, ApJ, 631, 280
Binney J. J., Tremaine S. D., 1987, Galactic Dynamics. Princeton Univ. Press, Princeton, NJ
Debattista V. P., Ferraras I., Pasquali A., Seth A., De Rijcke S., Morelli L., 2006, ApJ, 651, L97
Dehnen W., 2003, MNRAS, 265, 250
Freitag M., Amaro-Seoane P., Kalogera V., 2006, ApJ, 649, 91
Genzel R., Thatte N., Krabbe A., Kroker H., Tacconi-Garman L. E., 1996, ApJ, 472, 153
Genzel R., Eckart A., Ott T., Eisenhauer F., 1997, MNRAS, 291, 219
Genzel R. et al., 2003, ApJ, 594, 812
Ghez A. M. et al., 2005, ApJ, 620, 744
Kormendy J., Richstone D., 1995, ARA&A, 33, 581
Lauer T. R. et al., 1993, AJ, 106, 1436
Lauer T. R. et al., 1996, ApJ, 471, L79
Lauer T. R. et al., 2005, AJ, 129, 2138
Lynden-Bell D., 1979, MNRAS, 187, 101
Merritt D., 2001, ApJ, 556, 245
Merritt D., 2005, ApJ, 628, 673
Merritt D., 2006, Rep. Progress Phys., 69, 2513
Merritt D., Berczik P., Laun F., 2007, AJ, 133, 553
O'Leary R. M., Loeb A., 2007, MNRAS, submitted (astro-ph/0609046)
Peiris H. V., Tremaine S. D., 2003, ApJ, 599, 237
Press W. H. et al., 1992, Numerical Recipes in C, 2nd edn. Cambridge Univ. Press, Cambridge
Preto M., Merritt D., Spurzem R., 2004, ApJ, 613, L109
Rauch K. P., Tremaine S., 1996, New Astron., 1, 149
Reid M. J., Brunthaler A., 2004, ApJ, 616, 872
Reid M. J., Menten K. M., Trippe S., Ott T., Genzel R., 2007, ApJ, 659, 378
Salow R. M., Statler T. S., 2001, ApJ, 551, L49
Schödel R. et al., 2007, A&A, 469, 125
Toomre A., Toomre J., 1972, ApJ, 178, 623
Tremaine S. D., 1995, AJ, 110, 628
Yu Q., Tremaine S. D., 2003, ApJ, 599, 1129
Zhao H., Haennelt M. G., Rees M. J., 2002, New Astron., 7, 385

APPENDIX A: RELATING WORK AND ENERGY

Equation (6) gives the orbital energy of a star in the time-dependent potential. We show that the change in energy $\delta E_{\rm J}$ is a close relation to the mechanical work W given by equation (11). Recall that the time-integration is done in the approximation of a circular orbit. The general expression for the time-derivative of $E_{\rm J}$ in equation (4) is

$$\dot{E}_{\rm J} = \partial_t \Phi_{\rm bh}(\boldsymbol{r}, t) + \boldsymbol{v} \cdot \boldsymbol{\nabla}_r E + \dot{\boldsymbol{v}} \cdot \boldsymbol{\nabla}_v E. \tag{A1}$$

For a Hamiltonian system, the last two terms cancel out and $\delta E_{\rm J} = \partial_t \Phi_{\rm bh} \delta t$. This may not hold true once we integrate over a circular path. Keeping the angular speed constant, we have $\dot{\boldsymbol{v}} \cdot \boldsymbol{\nabla}_v E = 0$ so finite differentiation of equation (A1) gives

$$E_{\rm J}(\mathrm{d}t)|_{\rm c} - E_{\rm J}(0) = \partial_t \Phi_{\rm bh}|_{\rm c}\, \mathrm{d}t + \hat{\boldsymbol{\theta}} \cdot \boldsymbol{\nabla} \Phi_{\rm bh}\Big|_{\rm c} r \mathrm{d}\theta, \tag{A2}$$

where the subscript 'c' denotes quantities evaluated for a circular orbit, and we have taken the notation of equation (11). However, since $v_{\rm c} = r\dot{\theta}$ is constant, and $\dot{r} = 0$ by construction, we find $E_{\rm J}(\mathrm{d}t)|_{\rm c} - E_{\rm J}(0) = [\Phi_{\rm bh}(\mathrm{d}t) - \Phi_{\rm bh}(0)]_{\rm c}$ from equation (4). Hence

$$\delta E_{\rm J} = \int \partial_t \Phi_{\rm bh} \mathrm{d}t \approx \int \partial_t \Phi_{\rm bh}|_{\rm c}\, \mathrm{d}t = [\Phi_{\rm bh}(t) - \Phi_{\rm bh}(0)]_{\rm c} - W(t), \tag{A3}$$

where we have substituted for W from equation (11). This is the relation sought. Another approach would have taken into account $\ddot{\theta} \neq 0$ in equation (A1) for a better approximation to the orbit. This extra step was left out of the analysis as it did not lead to new insight.

APPENDIX B: DETAILS OF THE INTEGRALS

In this appendix, we sketch the path leading up to equation (9) and Fig. 2. Remembering equation (5), the partial derivative

$$\frac{\partial \Phi_{\rm bh}(\boldsymbol{r}, t)}{\partial t} = \dot{R} \frac{\partial \Phi_{\rm bh}(\boldsymbol{r}, t)}{\partial R} = \dot{R}\, \frac{G M_{\rm bh}}{(r^2 - 2xR + R^2)^{\frac{3}{2}}} (R - x) \tag{B1}$$

is set in the form of equation (9) after substituting for equation (5) with the dimensionless constant $\alpha \equiv R_{\rm o}/r$ and the solution $x(t) = r\ \cos\ (\omega_\star\ t)$. From equation (7), let $\omega = \nu\omega_\star$ and define the integration variable $\omega_\star\ \mathrm{d}t = \mathrm{d}\varpi$. The radical $\sqrt{1 - 2\alpha\ \cos(\varpi) \sin(\nu\varpi + \phi_{\rm o}) + \alpha^2 \sin^2(\nu\varpi + \phi_{\rm o})}$ matches a truncated Taylor series development whenever $\alpha \ll 1$. The development including the first three terms of the series proceeds from well-known algebra. Summing the first two terms of the series and substituting for

$\partial_t \Phi_{\rm bh}$, we find after integration

$$\delta E_{01}(\varpi) \simeq \frac{GM_{\rm bh}}{r}\alpha\nu\times\left\{\left(\frac{9\alpha^2}{16}-\frac{1}{2}\right)\left[\frac{\sin([\nu-1]\,\varpi+\phi_{\rm o})}{\nu-1}+\frac{\sin([\nu+1]\,\varpi+\phi_{\rm o})}{\nu+1}\right]+\frac{\alpha\cos(2\,\nu\,\varpi+2\,\phi_{\rm o})}{8\nu}-\frac{9\alpha^2}{16}\right.$$
$$\left.\times\left[\frac{\sin([3\,\nu-1]\,\varpi+3\,\phi_{\rm o})}{3\,\nu-1}+\frac{\sin([3\,\nu+1]\,\varpi+3\,\phi_{\rm o})}{3\,\nu+1}\right]+\frac{3\alpha}{16}\left[\frac{\cos([2\,\nu+2]\,\varpi+2\,\phi_{\rm o})}{\nu+1}+\frac{\cos([2\,\nu-2]\,\varpi+2\,\phi_{\rm o})}{\nu-1}\right]\right\}+O(\alpha^3). \tag{B2}$$

The third term of the series corresponds to the octopole of the potential. The integration was recovered with help from the MAPLE software v9.5 and 11; re-arranging the output and dropping all terms of the order of $O(\alpha^5)$ or higher, we obtain

$$\delta E_2(\varpi) \simeq \frac{GM_{\rm bh}}{r}\alpha\nu\times\left\{\frac{45\alpha^2}{64}\left[\frac{\sin([3\nu-1]\varpi+3\,\phi_{\rm o})}{3\,\nu-1}+\frac{\sin([3\nu+1]\varpi+3\,\phi_{\rm o})}{3\,\nu+1}\right]+\frac{15\alpha^3}{64}\frac{\cos(4\nu\varpi+4\phi_{\rm o})}{\nu}\right.$$
$$-\frac{15\alpha^2}{64}\left[\frac{\sin([\nu-3]\varpi+\phi_{\rm o})}{\nu-3}+\frac{\sin([\nu+3]\varpi+\phi_{\rm o})}{\nu+3}\right]-\frac{15\alpha^3}{32}\left[\frac{\cos([2\nu+2]\varpi+2\,\phi_{\rm o})}{\nu+1}+\frac{\cos([2\nu-2]\varpi+2\,\phi_{\rm o})}{\nu-1}\right]$$
$$-\frac{15\alpha^3}{16}\frac{\cos(2\,\nu\,\varpi+2\,\phi_{\rm o})}{\nu}+\frac{15\alpha^3}{64}\left[\frac{\cos([4\nu+2]\varpi+4\,\phi_{\rm o})}{2\,\nu+1}+\frac{\cos([4\nu-2]\varpi+4\,\phi_{\rm o})}{2\,\nu-1}\right]-\frac{45\alpha^2}{64}\left[\frac{\sin([\nu-1]\varpi+\phi_{\rm o})}{\nu-1}\right.$$
$$\left.\left.-\frac{\sin([\nu+1]\varpi+\phi_{\rm o})}{\nu+1}\right]+\frac{15\alpha^2}{192}\left[\frac{\sin([3\,\nu-3]\,\varpi+3\,\phi_{\rm o})}{\nu-1}+\frac{\sin([3\,\nu+3]\,\varpi+3\,\phi_{\rm o})}{\nu+1}\right]\right\}+O(\alpha^4). \tag{B3}$$

The energy of a star at time $t=\varpi/\omega_\star$ is then $E_{\rm J}(t)=E_{\rm J}(0)+\delta E_{01}+\delta E_2+O(\alpha^4)$. The leading term in equation (B2) has the parity of the sinusoid, and hence to a good approximation $\delta E_{01}\rightarrow-\delta{\rm E}_{01}$ when the phase angle $\phi_{\rm o}\rightarrow\phi_{\rm o}+\pi$. Similar expressions can be obtained for the azimuthal work W. Starting with equation (13), we have

$$W=-\int\boldsymbol{\nabla}\Phi_{\rm bh}(\boldsymbol{r},t)\cdot{\rm d}\boldsymbol{l}=\int\frac{GM_{\rm bh}}{||\boldsymbol{R}-\boldsymbol{r}||^2}\frac{\boldsymbol{R}-\boldsymbol{r}}{||\boldsymbol{R}-\boldsymbol{r}||}\cdot r{\rm d}\theta\hat{\boldsymbol{\theta}}=-\frac{GM_{\rm bh}}{r}\int\frac{\alpha\,\sin(\nu\varpi+\phi_{\rm o})\,\sin(\varpi)\,{\rm d}\varpi}{(1+\alpha^2\sin^2[\nu\varpi+\phi_{\rm o}]-2\alpha\sin[\nu\varpi+\phi_{\rm o}]\cos[\varpi])^{\frac{3}{2}}}. \tag{B4}$$

The radical in this equation may be expanded once again in a Taylor series: we regroup the first two terms to obtain the work associated with the monopole and quadrupole of the potential. This reads

$$W_{01}(\varpi)=-\frac{GM_{\rm bh}}{r}\frac{\alpha}{2}\frac{1}{1-\nu^2}\,\{(1+\nu)\sin([\nu-1]\varpi+\phi_{\rm o})+(1-\nu)\sin([\nu+1]\varpi+\phi_{\rm o})\}+O(\alpha^2). \tag{B5}$$

Here too we find for W_{01} the same sign change as δE_{01} when shifting the phase angle $\phi_{\rm o}$ by π. The third term of the Taylor series gives a contribution W_2, which reads

$$W_2(\varpi)=\frac{3}{8}\frac{GM_{\rm bh}}{r}\alpha^2\left\{\frac{\cos[2(\nu+1)\varpi+2\phi_{\rm o}]}{2(\nu+1)}-\frac{\cos[2(\nu-1)\varpi+2\phi_{\rm o}]}{2(\nu-1)}+\frac{3\alpha}{2}\left(\frac{\sin[(\nu+1)\varpi+\phi_{\rm o}]}{\nu+1}-\frac{\sin[(\nu-1)\varpi+\phi_{\rm o}]}{\nu-1}\right)\right.$$
$$\left.+\frac{\alpha}{2}\left(\frac{\sin[(3\nu-1)\varpi+\phi_{\rm o}]}{3\nu-1}-\frac{\sin[(3\nu+1)\varpi+\phi_{\rm o}]}{3\nu+1}\right)-\cos[2\varpi]\right\}+O(\alpha^3). \tag{B6}$$

The net work (in azimuth) is the sum of equations (B5) and (B6). All equations admit simplifications when integrating over one full revolution, $\varpi=0\rightarrow2\pi$. Thus, for example, equation (B5) simplifies to

$$W_{01}(2\pi)=-\frac{GM_{\rm bh}}{r}\frac{\alpha}{1-\nu^2}\,(\sin[2\pi\nu+\phi_{\rm o}]-\sin[\phi_{\rm o}]) \tag{B7}$$

when $\nu\neq1$, and $W_{01}(2\pi)=-GM_{\rm bh}\pi\cos(\phi_{\rm o})/r$ otherwise. Equation (B7) reduces to equation (13) for the harmonic potential once we substitute for ν from equation (8). Note that equations (B2) and (B3) are related to equations (B5) and (B6) through equation (A3).

This paper has been typeset from a TEX/LATEX file prepared by the author.